Q. J. R. Meteorol. Soc. (1997), **123**, pp. 1621–1652

Balanced mesoscale motion and stratified turbulence forced by convection

By G. K. VALLIS[1], G. J. SHUTTS[2]* and M. E. B. GRAY[2]
[1]*University of California, USA*
[2]*Meteorological Office, UK*

(Received 13 March 1996; revised 31 October 1996)

SUMMARY

Numerical experiments are carried out with a large-eddy simulation model to investigate the production of stratified turbulence and gravity wave energy in the atmospheric mesoscale by deep convection. Relatively long integrations (typically about 2.5 days) are carried out, so that statistical equilibrium might be achieved for an atmosphere subject to fixed cooling and a ground surface maintained at constant temperature. The main simulations may be considered as representing convective activity in a cold airstream passing over warm seas. The transfer of updraught kinetic energy into quasi-horizontal rotational energy, and its subsequent cascade to larger scales, is examined in the context of the production of balanced motion and stratified turbulence theory. Experiments are carried out to examine the effects of the Coriolis force, a wave-damping stratosphere, boundary-layer vertical wind shear, and precipitation.

An inverse mesoscale energy cascade is observed in experiments both with and without background rotation (the Coriolis effect), although weaker in the latter case. Mean boundary-layer vorticity is found to be the principal source of the horizontal rotational energy created by deep convection, although the dipole character of the vorticity thereby produced frustrates the inverse energy cascade. At the level of convective detrainment, potential-vorticity anomalies have a small monopolar element in the rotating case and this implies a direct forcing of energy at large scales. It also promotes a more efficient inverse energy cascade through long-range influence. The inverse energy cascade arises primarily because of the quasi-two-dimensional, divergence-free nature of the flow at scales larger than the convective forcing, which is maintained by the stable stratification. Even in the absence of background rotation balanced flow arises, especially in the upper troposphere and in the decay phase of the simulations when the surface fluxes and atmospheric cooling driving the convection are removed. In these cases potential-vorticity inversion can be quite successful in determining the other field variables, with contributions from both geostrophic and cyclostrophic balance. Suppression of precipitation (i.e. removing the liquid-water phase) increases the net convective mass transfer through the elimination of convective downdraughts, which leads to a higher efficiency of balanced-flow energy production and upscale energy transfer. Intense 'meso-vortices', with warm core structure, form spontaneously after about 2.5 days integration in these runs.

KEYWORDS: Deep convection Inverse energy cascade Large-eddy simulation Meso-vortices

1. INTRODUCTION

This paper concerns the general questions of what happens to the kinetic energy released by the buoyancy force in deep, penetrative convection in the atmosphere, and what is the nature of the mechanisms producing the observed mesoscale energy spectrum? The energy released in convection can in principle undergo three types of transition: it may be converted to three-dimensional turbulent energy then cascading to small scales and dissipating; it may be converted to gravity wave energy; or it may become 'balanced' quasi-two-dimensional flow, and cascade to larger scales in stably stratified turbulence, possibly associated with the production of stable vortices. The proportions of energy going into these different forms must vary considerably, depending on the form of convection that evolves and the environment in which the motion takes place. In the linear model of Schubert *et al.* (1980) only a few per cent of energy released was found to be retained after the geostrophic adjustment process was complete, depending on the ratio of the horizontal scale of the convection to the Rossby radius of deformation. In contrast, Shutts and Gray (1994) found that in two-dimensional numerical simulations, a single deep convective plume in a rapidly rotating environment could capture around 30% of the energy released in balanced flow. More recent simulations by Gray (1996) using a terrestrial value for the Coriolis

* Corresponding author: Meteorological Office, London Road, Bracknell, Berkshire RG12 2SZ, UK.

parameter have shown that up to 60% of the energy released may be retained in balanced structures—depending on how much mass is convected. The simulations have much in common with observed Mesoscale Convective Systems (MCSs) in which lower to middle tropospheric vortices are created. Simulations by Herring and Métais (1989) and Métais *et al.* (1994) indicate that in some circumstances (particularly when background rotation is present) balanced flow can be efficiently produced in a three-dimensional stratified medium by small-scale forcing, but their simulations are somewhat idealized, making the direct connection to the atmospheric mesoscale difficult.

Satellite imagery shows that convection has strong mesoscale organization in cold airflows over warm seas. This may take the form of shallow cellular organization in hexagonal patterns approximately 20 to 60 km across, or deep convective clusters with anvils up to 60 km across and individual clouds with similar spacing. The former process may be regarded as a boundary-layer phenomenon whereas in the latter the process is penetrative in the sense that updraughts extend far into the stably stratified environment. It seems likely that the time-scale of individual cloud systems is several hours (although that of an individual cloud may be shorter) and comparable with the Coriolis time-scale f^{-1}. As with the MCS, a proportion of the released energy may be retained in vortical motion derived either from the earth's rotation or boundary-layer wind shear.

Raymond and Jiang (1990) postulated that the longevity of the MCS was associated with the production of a positive potential-vorticity (PV) anomaly in the middle or lower troposphere caused by latent-heat release. The PV anomaly implies a balanced meso-vortex which, in the absence of strong background flow deformation, persists and is capable of inducing low-level ascent ahead of it. Using an axisymmetric balanced model, Shutts *et al.* (1988) showed that the production of PV anomalies follows directly from the convective mass transfer, and that lens-like regions of zero PV and frontal discontinuities of very high PV may be produced.

From a dynamical viewpoint, the net effect of deep, penetrative convection is equivalent to the effect of a particular distribution of mass sources and sinks in the flow (Ooyama 1971). If M_f is a hypothetical mass source term introduced into the continuity equation then it can be shown that Ertel's theorem for the conservation of potential vorticity, q, becomes:

$$\frac{\mathrm{D}q}{\mathrm{D}t} = -qM_f \tag{1}$$

implying that mass sources lower the PV and mass sinks increase it. The process is related to the notion of dilution and concentration of PV substance introduced by Haynes and McIntyre (1990).

The production of balanced mesoscale motion may have an impact not only on the mesoscale itself, but also on synoptic and larger-scale flows, if the energy can be transferred to larger scales. It is observed that the slope of the atmospheric energy spectrum changes from a k^{-3} spectrum (where k is the horizontal wave number) at larger scales to a spectrum more nearly that of $k^{-5/3}$ for scales smaller than a few hundred kilometres (e.g. Gage and Nastrom 1986). The large-scale spectrum may be understood in terms of quasi-geostrophic turbulence (e.g. Charney 1971): the twin constraints of energy and enstrophy conservation combine to produce a direct cascade of enstrophy to small scales, characterized by a -3 spectrum of the three-dimensional wave number. Although various simulations of two-dimensional turbulence at high resolution do frequently yield spectra steeper than k^{-3} (e.g. Maltrud and Vallis 1991) it is generally thought that the large-scale spectrum is indeed characterized by an enstrophy cascade to smaller scales (e.g. Boer and Shepherd 1983). The mechanisms producing the $k^{-5/3}$ mesoscale spectrum are less clear, since the horizontal scale is still too large to be associated with isotropic three-dimensional turbulence. Two

mechanisms suggest themselves, one being associated with gravity waves. In this scenario, in addition to an enstrophy cascade of rotational modes, there may exist a weaker direct cascade of energy (i.e. from large to small scales) associated with divergent (or, more generally, unbalanced) modes, as well as the possible direct excitation of internal waves at these scales (Van Zandt 1982). Such internal waves will tend to produce a shallower spectrum—perhaps close to k^{-2}, which is similar to $k^{-5/3}$; this may dominate at smaller scales. Recent simulations of the shallow-water equations (Yuan and Hamilton 1994) also give some credence to this idea, or similar ideas.

Another possibility is that the spectrum is due to an *upscale* transfer of energy associated with stratified turbulence in the mesoscale (Lilly 1983). The idea is that, for the low Froude number (Fr) flows, characterizing the mesoscale, 'two-dimensional' flow is the lowest order balanced approximation (see Riley *et al.* (1981) and Vallis (1996) for a discussion of the scaling). The flow is not properly two-dimensional, since there can be large variations in the vertical, but each horizontal layer obeys the two-dimensional vorticity equation. We will refer to such motion as 'quasi-horizontal'. A source of energy (e.g. convection at the scale of tens of kilometres) will then produce an inverse energy cascade with a concomitant energy spectrum close to $k^{-5/3}$. If this is true, then smaller-scale convective motion could have a direct influence on the larger-scale motion. It is this latter mechanism that we shall be primarily concerned with in this paper. Interestingly, Herring and Métais (1989) were unable to obtain a robust inverse energy cascade in simulations of forced stably stratified turbulence. When rotation was added to such simulations a more effective inverse energy-cascade was obtained (Métais *et al.* 1994), with a Froude number ~ 0.2 and Rossby number ~ 0.1. Furthermore, whether quasi-horizontal motion is in fact a self-consistent limit of the highly stratified equations is unclear, since each horizontal layer moves independently in this limit and the motion may be unstable. The question of whether balanced mesoscale motion and inverse cascades exist is thus of both practical and theoretical interest.

If an upscale cascade of energy does take place, then at some intermediate scale it must 'collide' with the forward (downscale) enstrophy cascade (Lilly 1989). Simulations by Maltrud and Vallis (1991) indicate that the cascades are in fact largely transparent to each other, and produce only a change in spectral slope at some intermediate scale, much as is observed. The mechanisms of each cascade are evidently essentially independent of each other, probably because different triad interactions are involved in each cascade. For this reason we are able to study any upscale energy transfer independent of the downscale enstrophy transfer, enabling a mesoscale model of limited horizontal extent (in our case typically 300 km) to be usefully employed.

It is the purpose of this paper to investigate, by numerical simulation, whether deep convective clouds that occur in cold airstreams over warm seas can indeed force an upscale energy transfer through the creation of quasi-barotropic mesoscale eddy motions. A range of experiments are performed which elucidate the role of the Coriolis force, boundary-layer wind shear, and precipitation-induced downdraughts.

In the next section, the model we use and the experimental set-up are briefly described. This is followed by a description of the main numerical results. In section 4 we examine more closely the production of balanced motion. Section 5 concludes with a discussion of the relevance of this study to predictability issues.

2. Model formulation and experiment design

Our goal is to provide a crude model of the kind of convection that occurs, for example, in a cold-air outbreak, when a cold polar airstream flows over a warm ocean. Two

approaches to modelling this phenomenon are possible: firstly, one could imagine that the model domain was following the airstream over warmer seas, and represent this effect by specifying a time-dependent sea surface temperature. Alternatively, one could consider the domain to be fixed over a patch of ocean for which the sea surface temperature is constant, and represent the advection of cold air into the domain by an apparent cooling function. The latter approach is the one adopted here, principally because it allows a statistically steady state to be reached. The end of the cold-air outbreak is modelled simply by cutting off the parametrized surface fluxes and atmospheric cooling in the model, which results in a decay or spin-down phase of the simulations more similar to previous integrations on stratified turbulence (e.g. Herring and Métais 1989).

The process envisaged here is clearly not a good model of cold, continental air masses flowing from land to sea, since these are characterized by a deepening convective boundary layer rather than convective systems extending throughout the troposphere. Rather, one might regard the cold air mass as having been over the sea for many days and responding to higher sea temperatures and a cyclonic flow environment. Such synoptic situations are not uncommon over the eastern side of the Atlantic and Pacific Oceans in middle/high latitudes during the winter.

The numerical model itself is a 'large-eddy simulation' model, described more fully in Shutts and Gray (1994). It is based on the non-hydrostatic anelastic equations (e.g. Ogura and Phillips 1962), contains water vapour and Richardson-number-dependent subgrid-scale parametrizations for dissipation and boundary-layer transfer. The equations of motion are:

$$\frac{\mathrm{D}\mathbf{v}}{\mathrm{D}t} + f\mathbf{k}\times\mathbf{v} = -\nabla\frac{p'}{\widehat{\rho}} + g\frac{\theta_v'}{\widehat{\theta}} + \frac{1}{\widehat{\rho}}\nabla\tau \tag{2}$$

$$\frac{\mathrm{D}T_L}{\mathrm{D}t} = -\frac{L_v S_R}{C_p} + \frac{1}{\widehat{\rho}}\nabla(\widehat{\rho}F_T) \tag{3}$$

$$\nabla\cdot(\widehat{\rho}\mathbf{v}) = 0 \tag{4}$$

$$\frac{\mathrm{D}r_T}{\mathrm{D}t} = -S_R + \frac{1}{\widehat{\rho}}\nabla(\widehat{\rho}F_r) \tag{5}$$

$$\frac{\mathrm{D}r_R}{\mathrm{D}t} = \frac{1}{\widehat{\rho}}\nabla(\widehat{\rho}F_R) + \frac{1}{\widehat{\rho}}\frac{\partial}{\partial z}(\widehat{\rho}r_R w_R) + S_R \tag{6}$$

$$p = \rho R T_v = \rho R T(1 + 0.608r) \tag{7}$$

$$\theta_v = T_v\left(\frac{p_{\mathrm{ref}}}{p}\right)^{\kappa} \tag{8}$$

$$T_L = T + (gz - L_v r_L)/C_p \tag{9}$$

In these equations, $\mathbf{k}$ is a unit vector in the z direction and the variables $\mathbf{v}$, p, T, T_L, T_v, θ_v and ρ are three-dimensional vector wind, pressure, temperature, liquid water temperature, virtual temperature, virtual potential temperature and density. A hat over a variable (e.g. $\widehat{\rho}$) indicates a reference profile (a function of z only) and primes denote the deviation from this. Also, r, r_R, r_L, r_T are the vapour, rain, liquid water and total water mixing ratios respectively; g is gravitational acceleration, R is the gas constant for dry air, C_p is the specific heat at constant pressure and $\kappa = R/C_p$; w_R is the fall speed of rain and L_v is the latent heat of vaporization. The turbulent shear stress τ, and the turbulent fluxes of T_L, r_T and r_R (F_T, F_r and F_R respectively) are all based on a Smagorinsky–Lilly parametrization as described by Shutts and Gray (1994). A simple, 'warm' cloud microphysical scheme (Kessler 1974) represents the processes of autoconversion of cloud

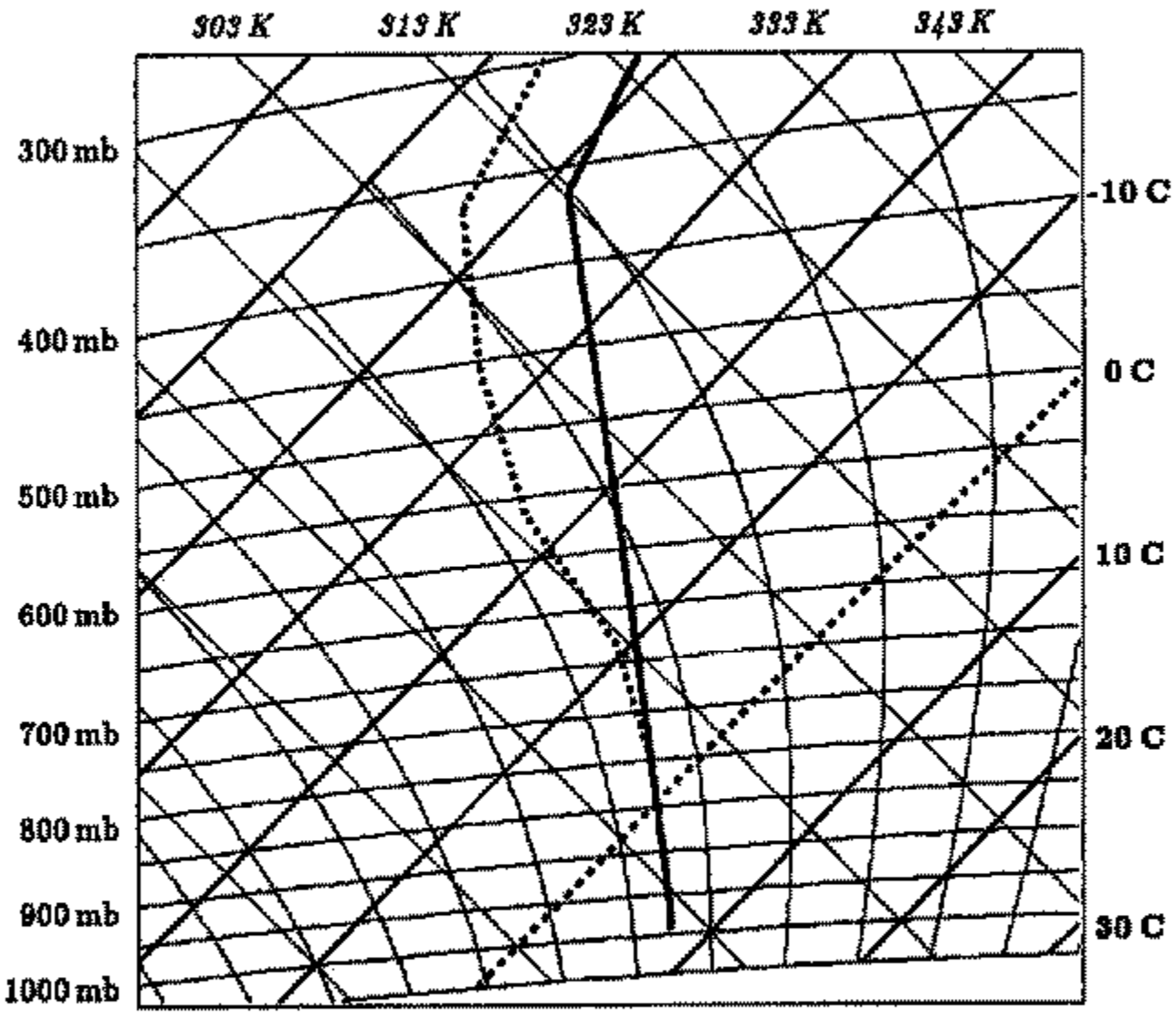

Figure 1. Tephigram showing the initial thermodynamic profile for all model integrations; solid line is temperature, dashed line is dew-point. Notice the stable layer above 350 mb which serves to arrest convective updraughts before reaching the model lid at $z = 10$ km.

droplets to rain, accretion of cloud droplets onto rain, and evaporation of rain into dry air—collectively represented by the term S_R.

The advection terms in the momentum and thermodynamic equations are computed on an Arakawa C grid, using the 'ULTIMATE' advection scheme on all model variables (Leonard 1991). Each horizontal slice employs cyclic boundary conditions and comprises 300×300 points with 1 km spacing; vertical levels are spaced unevenly to afford greater resolution in the boundary layer. The primary model levels (holding p, u, v and T_L) are located at heights of 47, 234, 793, 1756, 3035, 4500, 6049, 7626 and 9208 metres. Vertical-velocity levels lie roughly midway between the main levels (above 1 km) and rigid-lid boundary conditions are defined by setting $w = 0$ at $z = 0$ and $z = 10$ km. A no-slip lower boundary is enforced by requiring zero wind on a fictitious subterranean main level.

Where appropriate, the Coriolis parameter assumes a typical mid-latitude value of 10^{-4} s^{-1}. In all cases the sea surface temperature was fixed at 291 K (18 °C) and the initial atmospheric temperature profile was determined by a temperature of 281 K at level 2 ($z = 234$ m) and a constant squared buoyancy frequency of 1.4×10^{-4} s^{-2} up to $z = 7626$ m—above which the temperature profile was set to be strongly statically stable. The effect of this shallow stable layer was to ensure that the neutral buoyancy level (based on parcel theory) of near-surface air parcels lay within the model atmosphere. A tephigram depicting the temperature and dew-point of the initial state is shown in Fig. 1. A prescribed diabatic cooling rate of 10^{-4} K s^{-1} (≈ 8.6 degC per day) is applied on all model levels except those at the top and bottom—the latter of which is diagnostic.

In order to ensure strong turbulent heat and moisture transfer from the surface, a basic uniform wind U is assumed in the x direction above the surface (e.g. Rotunno *et al.* 1988). This is achieved straightforwardly in the rotating case (i.e. with the usual value of the Coriolis parameter). In these experiments the basic flow is geostrophically balanced through the inclusion of a fixed, constant pressure gradient in the y direction. In this sense the basic flow is continually driven towards the geostrophic value by the fixed applied pressure gradient and, because of the imposition of a no-slip condition at the surface, a shear is

maintained across the boundary layer. Some care is required in defining the corresponding experiment with no background rotation. If the Coriolis parameter were simply set to zero everywhere, there would then be no imposed constant pressure gradient since there would be no requirement for geostrophic balance, and nothing to maintain a lower-level shear. Under these circumstances, turbulent boundary layer and convective momentum transport would drain away x-momentum so that statistical equilibrium would only be achieved when the momentum in the initial basic-state flow was removed. This clearly is a very different physical problem from that of deep convection in a geostrophically balanced uniform flow where Coriolis torque on the horizontally averaged flow counterbalances the net momentum sink (e.g. as in the Ekman boundary layer). The boundary-layer shear may also be important in organizing the convection, without itself being an important source (on average) for vertical velocity (C. Snyder, personal communication).

Thus, in order to keep the rotating and non-rotating simulations as similar as possible in terms of the convective forcing and boundary-layer fluxes, our 'zero Coriolis force simulations' allow a Coriolis effect on the horizontally averaged flow but not on the perturbed flow. That is, the Coriolis term $f\mathbf{k} \times \mathbf{V}$ is replaced by $f\mathbf{k} \times \overline{\mathbf{V}}$ where the overbar on $\mathbf{V}$ denotes the horizontal average across the entire domain. With this modification only the mean flow is subject to the Coriolis force. This enables us to study the effect of the Coriolis force on the perturbed flow. As in the full rotating case, a constant pressure gradient in the y direction is required to maintain geostrophic balance, and this maintains a low-level shear. Note that the mean flow can, and does, depart from geostrophy on each level. The largest departure of the mean flow from its geostrophic value occurs in the boundary layer. This scheme may be regarded as a device to maintain a shear across the boundary layer, and hence to keep the transfer of moisture and momentum across the boundary layer similar to that in the rotating case.

Horizontal vorticity diffused away from the lower boundary is a potential source of vertically oriented vorticity in deep convection. To investigate the effect of this, a simulation is carried out in which the horizontally averaged wind is fixed at its initial imposed value. This does not suppress surface heat and momentum fluxes since the no-slip condition is still enforced at the model level notionally below ground.

The simulations with a rigid lid at 10 km do not, naturally enough, allow gravity waves to propagate into a stratosphere and dissipate. Nor, because of the limited horizontal extent and periodicity of the simulations, do they allow gravity waves to propagate away from their source. Thus, we can expect the geostrophic adjustment process to be artificially constrained. To overcome this, in some experiments a stratospheric gravity wave damping layer was included, by imposing Newtonian relaxation on all variables in the stratospheric part of a vertically extended model domain. To achieve this it was necessary to reduce the horizontal domain size to stay within computer memory bounds. In these experiments the build-up of gravity wave 'box modes' is alleviated and gravity wave energy may drain away to low levels, as it would in an unbounded flow.

Finally, the effect of precipitation on the long-term evolution of convection was investigated by performing integrations with no liquid water; condensed water is removed at the instant it is diagnosed by the model and so cloud and precipitation never form. Latent heat of condensation is, however, realized. The main consequence of this physics modification is that evaporation of rain and the generation of convective downdraughts cannot occur.

3. Results

In this section we describe the phenomenology of the main simulations, and diagnose the production of stratified turbulence and upscale energy transfer of the rotational flow. A

more detailed investigation of the nature of the balanced motion, and explicit PV inversions, are deferred to section 4.

(*a*) *Control integration*

Consider first the form of the convection produced after 75 000 s of integration (~1 day). Within the boundary layer at a height of 458 m, the vertical-velocity field shows an interesting mixture of cells and 'cuspy' lines oriented NE–SW (Fig. 2(a)) similar in form to those appearing in the squall-line simulations of Skamarock *et al.* (1994). The south-eastern side of the lines (where there is system-relative inflow) has upward motion of about 3 m s^{-1}: downdraughts of equal magnitude are found on the north-western side. The vertical velocity at $z = 5.27$ km is dominated by updraught cores a few kilometres in diameter that tend to aggregate along the cuspy lines seen in the boundary layer and with a range from -3.9 to 16.9 m s^{-1} (Fig. 2(c)). Higher up at $z = 8.42$ km the updraughts have terminated and circular patterns of gravity waves can be seen spreading outwards from the location of convective cells. The perturbation potential-temperature field (Fig. 2(b)) at $z = 234$ m suggests the formation of cool pools immediately behind the updraughts in response to cooling by the evaporation of precipitation.

After one day of model integration the effect of the Coriolis force acting on the remnants of earlier convection should be evident. Since detraining convective mass acts to dilute ambient potential vorticity (1), attention is focussed on the production of quasi-balanced motion at the model level nearest to the neutral buoyancy level. For highly stratified flow, the balanced flow is synonymous with the two-dimensional evolution of the rotational component of the horizontal flow (Lilly 1983). Although the presence of background rotation imparts some vertical stiffness to the flow, leading to flow evolution described by equations similar to the quasi-geostrophic set (Vallis 1996), if the flow is highly stratified the purely two-dimensional flow will still comprise the dominant part of the balanced flow. (These aspects of balance are explored further in section 4.) Here, we note that the flow is indeed highly stratified, and it is expedient to simply decompose the horizontal wind at $z = 7.6$ km into rotational and divergent components and then form the kinetic energy spectra of each. In addition, the kinetic energy spectrum of the vertical motion, and the available potential energy spectrum, are computed. Here the available potential energy (APE) is defined as:

$$\mathrm{APE} = \frac{g}{2B}\left(\frac{\theta'}{\widehat{\theta}}\right)^2 \tag{10}$$

where B is the constant, reference-state stability $\widehat{\theta}^{-1}\mathrm{d}\widehat{\theta}/\mathrm{d}z$.

Figure 3(a) shows these energy spectra plotted on a logarithmic scale. At this time (75 000 s) both the divergent kinetic energy and the APE exceed the rotational kinetic energy. The kinetic energy of the vertical motion is very much smaller than the sum of rotational and divergent energy spectra for all scales greater than the near grid-scale. This would be consistent with the use of the hydrostatic assumption everywhere except in the convective updraughts. Whilst it may be expecting too much to find an inertial sub-range power law in the energy spectrum, since the spatially localized nature of forcing by deep convection implies a broad spectral forcing, the slope of the spectrum is in fact not far removed from $k^{-5/3}$ on average. It is the rotational modes that we expect to persist after convection has ceased, and so here we shall tend to equate the rotational energy with quasi-balanced dynamics (see section 4 for further details). Inspection of the vorticity field at $z = 7.6$ km reveals dipolar (or more complex) patterns at convective updraught lines. The energy spectra at $t = 175\,000$ s are shown in Fig. 3(b). The rotational energy has increased

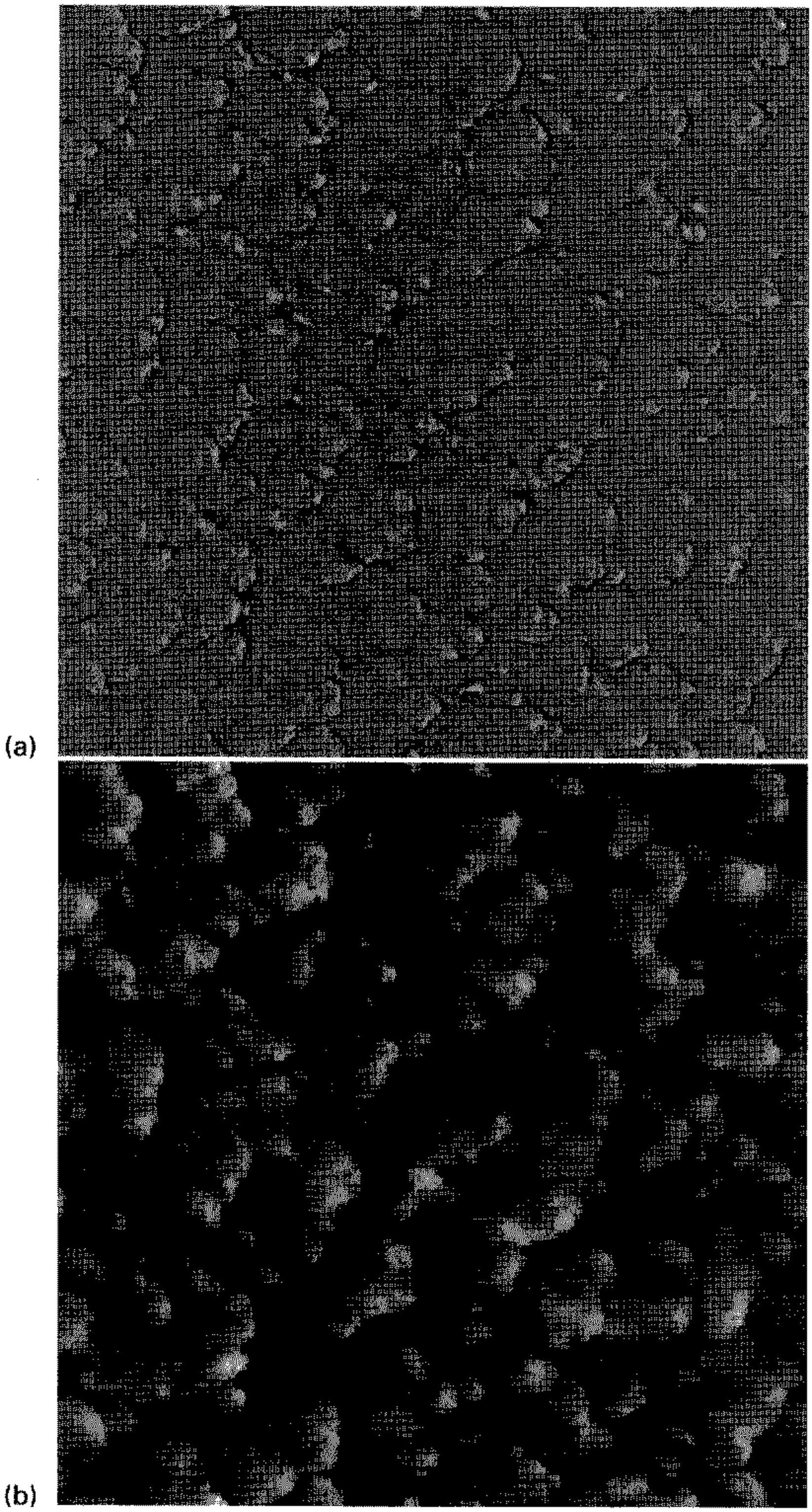

Figure 2. (a) Vertical velocity (range: $-3.1 \rightarrow +3.1$ m s^{-1}) at $z = 458$ m. (b) Potential-temperature perturbation (range: $3.8 \rightarrow 6.9$ degC) at $z = 234$ m. (c) Vertical velocity (range: $-3.9 \rightarrow +16.9$ m s^{-1}) at $z = 5.27$ km. In the above plots $t = 75\,000$ s and high values are black.

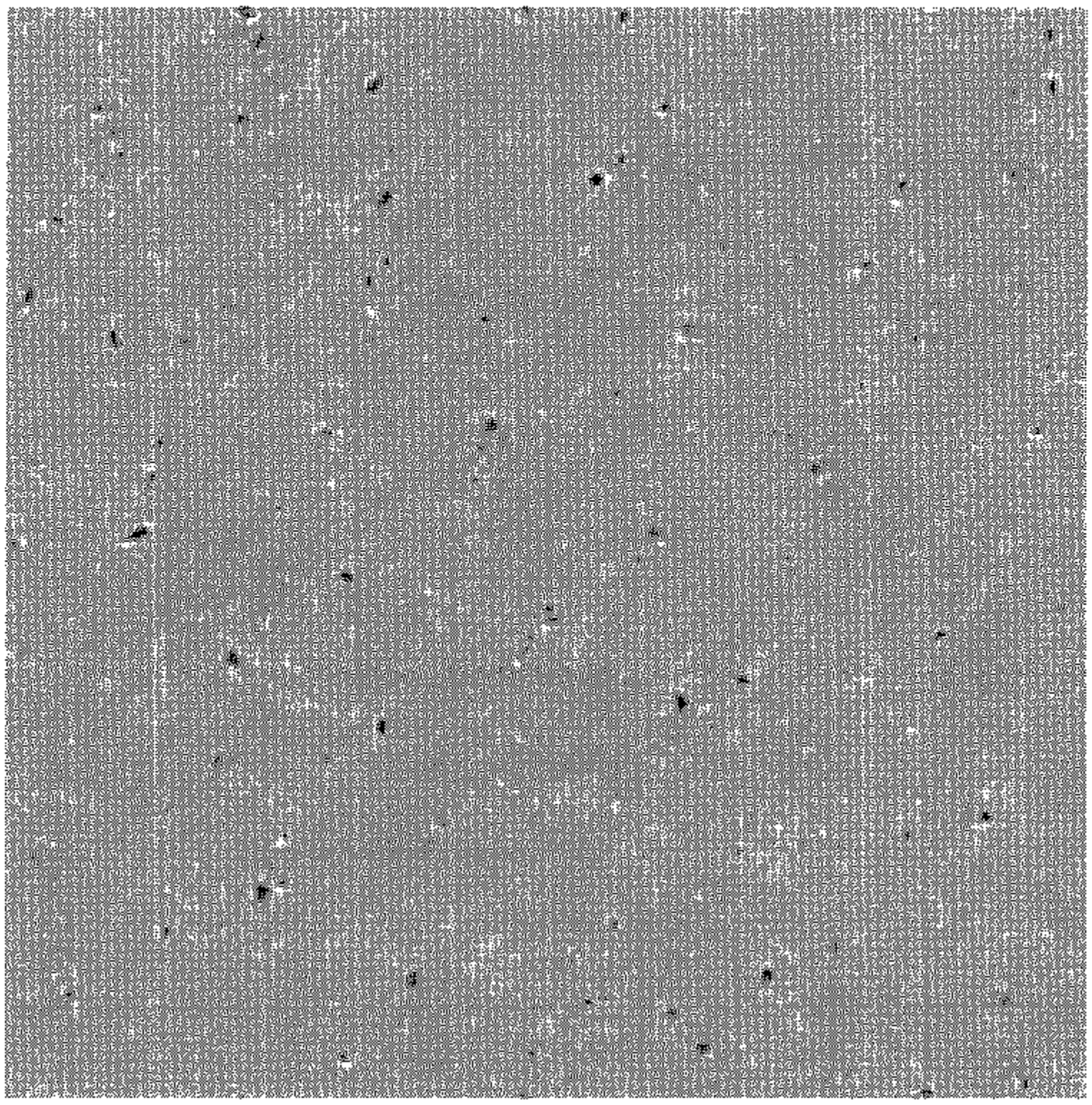

(c)

Figure 2. Continued.

further and is now comparable in magnitude with the divergent energy at a scale of around 50 km.

In order to quantify the level of stratified turbulence generated by deep convection over this two-day period, and to show its adjustment when convection ceases, the integration was continued with the diabatic cooling and surface energy/moisture fluxes set to zero after $t = 190\,000$ s. Figure 4 shows the total rotational kinetic energy and enstrophy at $z = 7.6$ km between $t = 100\,000$ and 300 000 seconds. Notice that up until the point where the convective forcing is switched off, both energy and enstrophy are still increasing: this may reflect the fact that the upscale energy transfer is blocked at the scale of the domain and that dissipation is very small for the gravest modes. During the 30 000 s period after the diabatic cooling and surface energy fluxes are switched off, the energy and enstrophy substantially reduce in magnitude. However, whilst the total rotational energy only falls by a little over 50% of its maximum value, the enstrophy falls by 95%. This behaviour is characteristic of the 'selective decay' properties of two-dimensional turbulence.

The vorticity field at $t = 350\,000$ s, $z = 7.6$ km is shown in Fig. 5. Now that the vorticity perturbations associated with the convection itself have decayed, there remains a background flow reminiscent of two-dimensional turbulence simulations (e.g. Maltrud and Vallis 1991), with the vorticity field beginning to organize itself into coherent vortices. A plot of the energy spectra at the same time (Fig. 6) shows that the rotational energy dominates the total energy and so the dynamics fit the two-dimensional turbulence paradigm well.

At this stage the rotational energy falls off at a rate faster than k^{-3} and most is trapped in scales greater than 30 km. Whilst the vertical coherence of the vorticity field on model

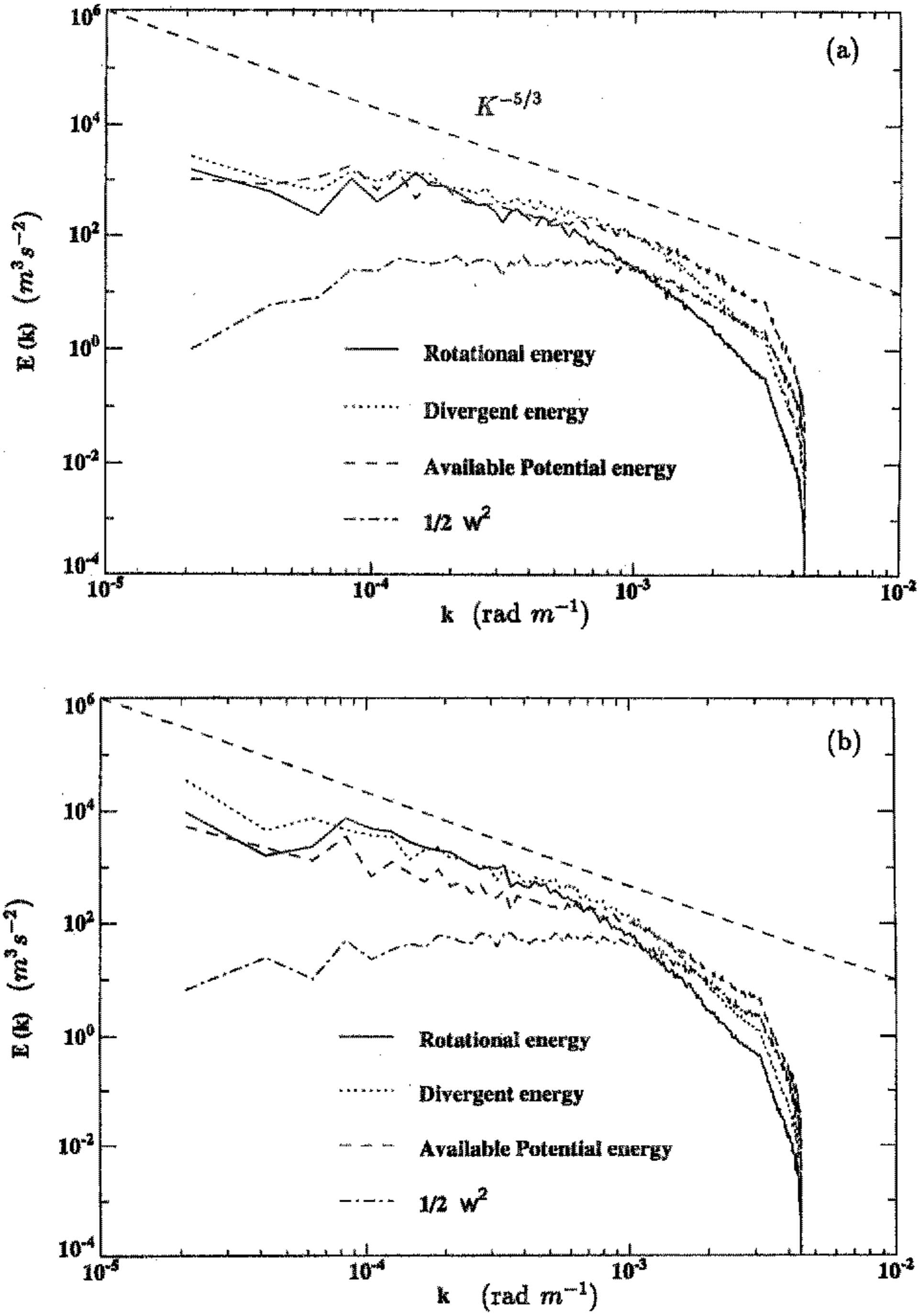

Figure 3. Energy spectra in the control integration at (a) $t = 75\,000$ s and (b) $t = 175\,000$ s. See text for energy definitions.

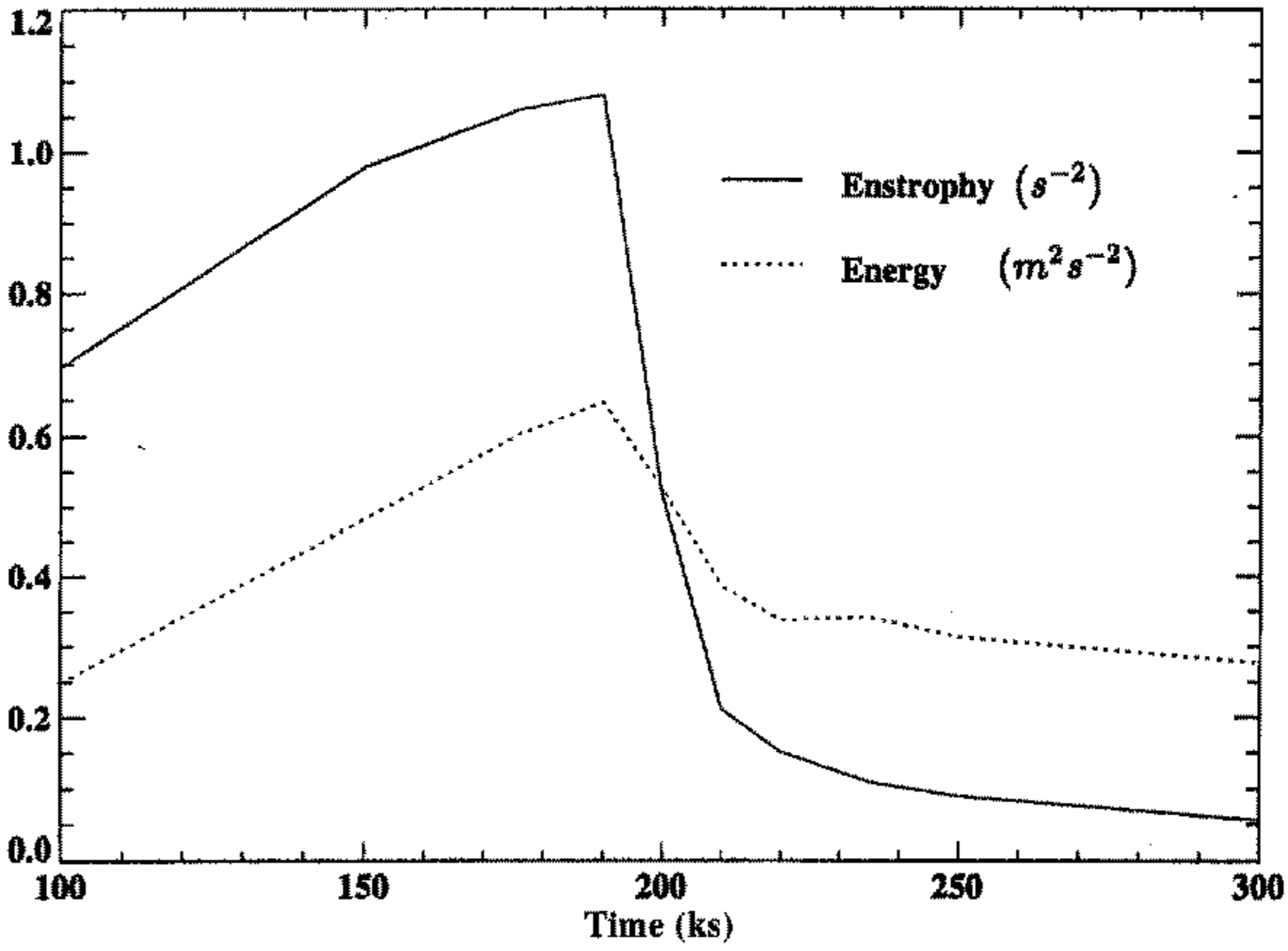

Figure 4. Graphs of the total rotational kinetic energy and enstrophy at $z = 7.6$ km plotted against time between 100 000 and 300 000 s. Both surface energy fluxes and the fixed domain cooling are switched off at $t = 190\,000$ s. Note the rapid decay of the enstrophy compared with the energy.

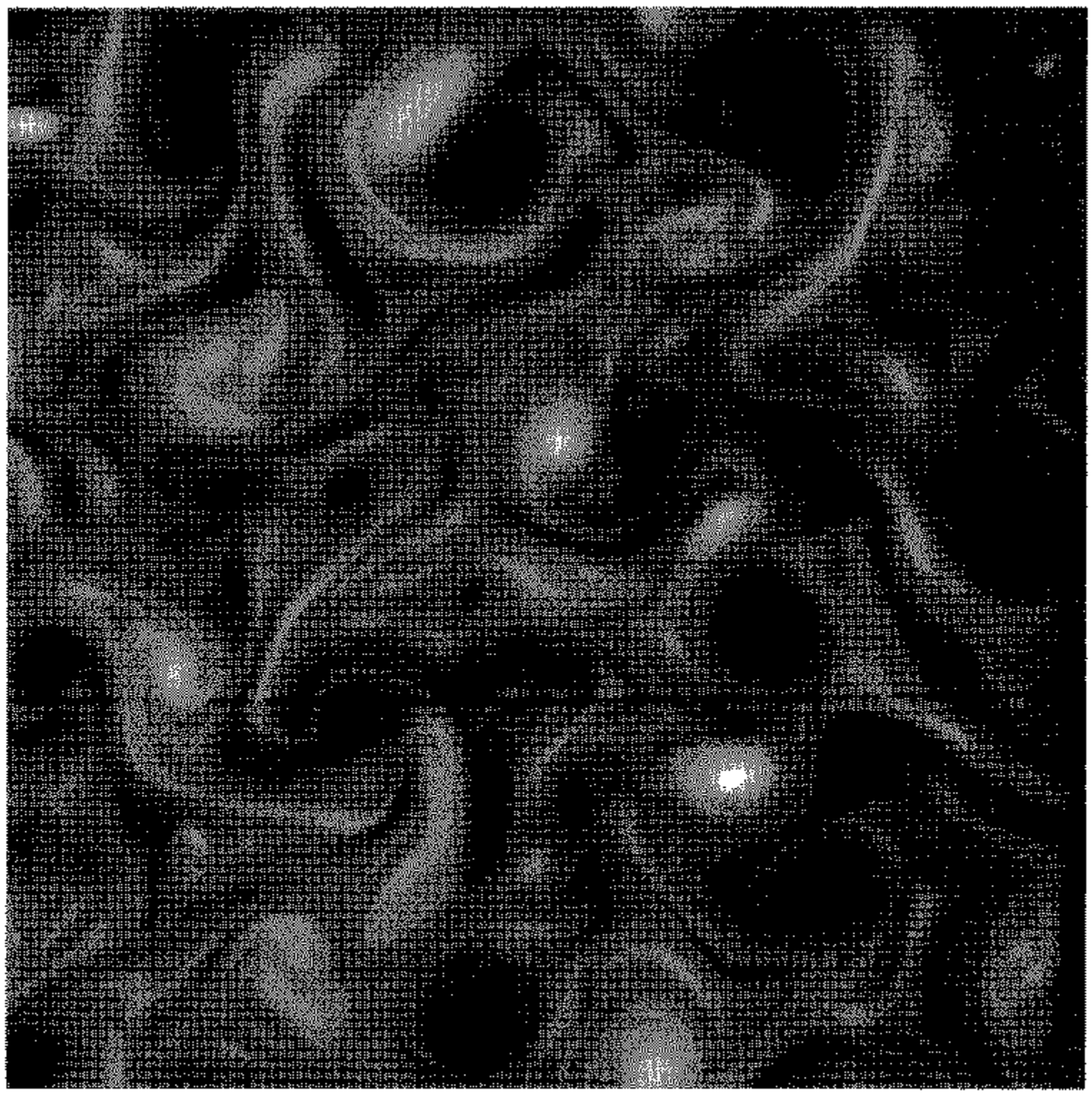

Figure 5. Vorticity field (range: $-3.2 \times 10^{-4} \rightarrow +3.6 \times 10^{-4}$) at $z = 7.6$ km, $t = 350\,000$ s in the control integration.

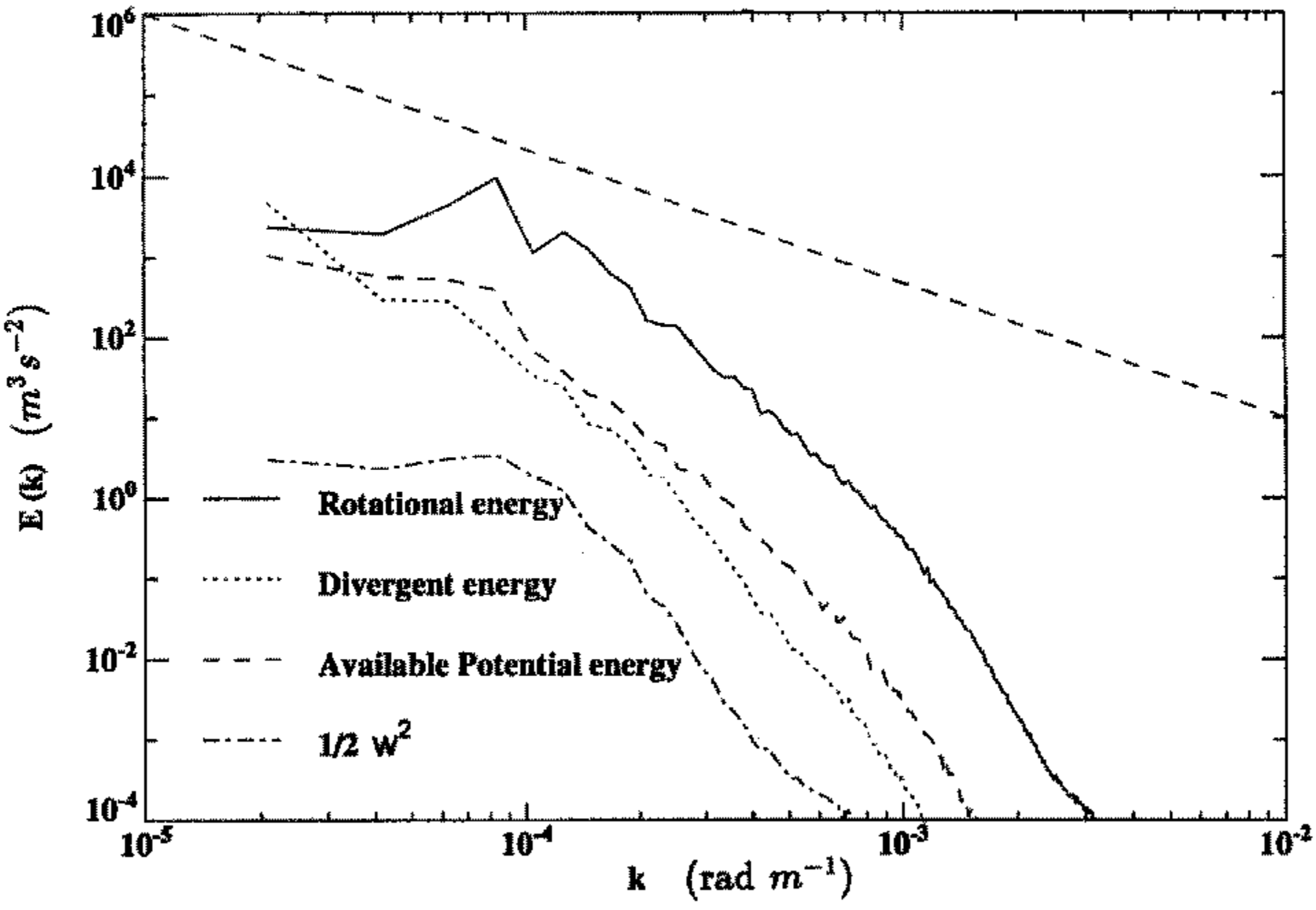

Figure 6. Energy spectra at $z = 7.6$ km, $t = 350\,000$ s in the control integration. This time is 125 000 s into the decay phase of the simulations. See text for energy definitions.

levels at heights 6.05 and 7.6 km is fairly high, the vorticity at $z = 4.5$ km is barely similar to that at 7.6 km. In two-dimensional stratified turbulence each horizontal layer will, in principle, evolve independently of the others, thus producing a decoupling of the vorticity field over shallow layers. This effect will be constrained by the necessity to maintain a sufficiently large Richardson number $(N^2/(\mathrm{d}u/\mathrm{d}z)^2)$: if the Richardson number becomes too small because the vertical shear of the horizontal flow becomes large, small-scale instability will arise which may provide some degree of dissipation and would prevent further decoupling. A small Richardson number would also normally imply a large Froude number, which would in fact vitiate the scaling on which the quasi-horizontal motion is based. The presence of background rotation will also help to maintain vertical coherence. Here, the Rossby number (defined by $Ro = U/fL$ where U and L are characteristic wind speed and horizontal length-scales) of the flow is of order unity, e.g. $U = 1$ m s^{-1} and $L = 10$ km at $z = 7.6$ km imply $Ro = 1$. However, the Rossby number is small for the largest scales in the domain for which $L \sim 50$ km. The Froude number (defined by $Fr = U/NH$ where H is a characteristic depth-scale of the flow) is also very small, e.g. since $H \sim 3$ km, $Fr \sim 0.03$. With these values, $Fr/Ro << 1$.

In cases where Ro is small, the buoyancy $b = g\theta'/\widehat{\theta}$ scales as fLU/H, consistent with the thermal-wind relation. The ratio of APE $(b/N)^2$ to the kinetic energy U^2 can then be straightforwardly shown to be $(Fr/Ro)^2$. If Ro is O(1) or larger, then b scales as U^2/H, and the APE/kinetic energy ratio is simply $(Fr)^2$. In our simulations (both rotating and not) this ratio is small, meaning the flow becomes dominated by kinetic energy (consistent with the energy spectra at this time) and, as discussed in section 4, satisfies the two-dimensional vorticity equation.

(*b*) *Coriolis force removed*

With the Coriolis force removed, much of the early organization of the convection is similar to the control (i.e. rotating) integration; noticeable differences emerge after about one day of integration. The energy spectra at $t = 75\,000$ s and $t = 175\,000$ s are shown in Figs. 7(a) and (b) respectively. These show that at the largest scales of the domain (i.e. wavelengths between 100 and 300 km) there are one to two orders of magnitude more divergent energy and APE than rotational energy (compare Figs. 3 and 7(a)). For wavelengths greater than about 60 km there is considerably more rotational energy in the control integration than in the integrations without background rotation, implying a more efficient inverse cascade or differences in the 'forcing function' (i.e. the nature of the convectively generated vorticity), or both. The evolution of the rotational kinetic energy spectra at 50 000 s intervals can be seen in Fig. 8. There is evidence of a slowing down in the build-up of energy in the largest scales of motion, since the curves at $t = 125\,000$ s and $t = 175\,000$ s are quite similar.

The main difference between the vorticity fields in the non-rotating and rotating cases is the appearance of larger-scale, single-signed features in the latter. In the non-rotating simulations, the boundary-layer shear gives rise to horizontal vortex tubes. Since (at least in the inviscid limit) vortex lines are 'frozen' to the flow, updraughts can pull these tubes upward, and such 'vortex twisting' will lead to the creation of a vertically oriented vorticity dipole. But if, additionally, there is some background rotation, vortex stretching can concentrate the background vorticity around the updraughts, giving a small monopolar component to the forcing vorticity field. To investigate the possible effect this has on the upscale energy transfer, independently of the efficiency of the production of balanced energy, we performed some integrations with a purely two-dimensional model. The evolution equation for this is:

$$\frac{\partial \zeta}{\partial t} + \mathbf{v} \cdot \nabla \zeta = F - D \tag{11}$$

where $\zeta = \mathbf{k} \cdot \text{curl } \mathbf{v}$, $\nabla \cdot \mathbf{v} = 0$, and F and D represent forcing and dissipation terms. For the dissipation we use a conventional harmonic viscosity. For the forcing we distribute small vortices at random locations throughout the domain, roughly simulating the vortex forcing of the main simulations. The vortices have a finite lifetime, over which the vorticity forcing is held fixed at the particular locations. The vortices are allowed to die, and new ones are allowed to form elsewhere. We use two forms for the vortices—either a pure dipolar form, or a dipolar form plus a weak monopolar component; the latter is a factor of 100 weaker than the dipole. The integration uses an energy–enstrophy conserving gridded code in a periodic domain, typically with 256 grid points on the side.

Figure 9 shows the evolution of the energy spectrum in these simulations. It is clear that energy at large scales can grow much more efficiently in the simulations with monopolar forcing. The distribution of monopoles itself provides forcing at large scales; further, the stream function induced by the monopolar component has a much greater far-field influence, whereas that of a dipole is confined to the neighbourhood of the disturbance itself, inhibiting turbulent interactions. These results imply that the diminished transfer of energy to large-scale in the non-rotating runs may be caused, in part, by the nature of the forcing itself, and not simply because the addition of the Coriolis force enhances the two-dimensionality of the flow via the production of geostrophically balanced flow.

(*c*) *Without rotation: fixed horizontally averaged wind*

In the simulation without rotation, not only was the Coriolis parameter set to zero but also the horizontally averaged wind was held fixed at its initial value on all model levels.

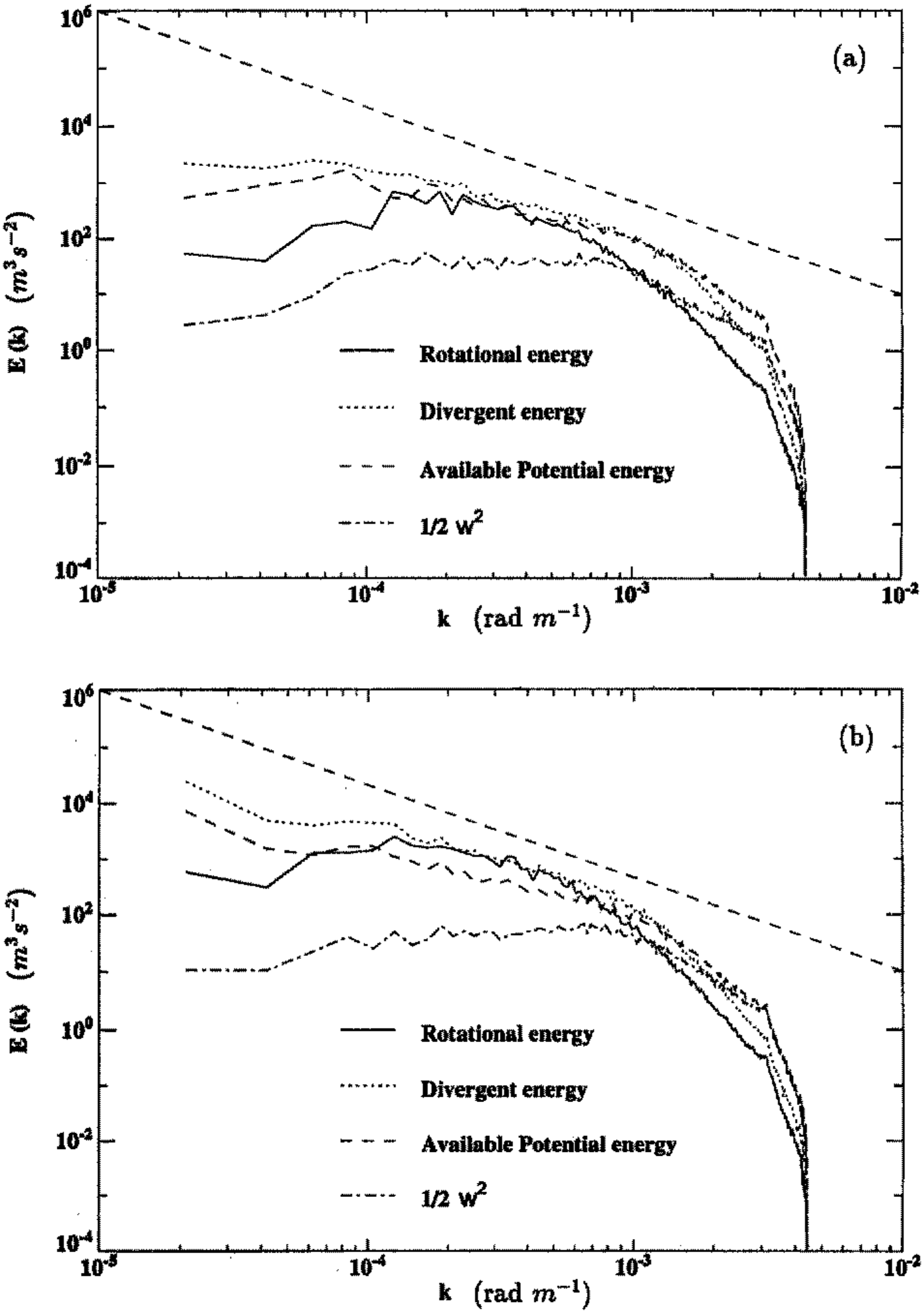

Figure 7. Energy spectra at $z = 7.6$ km in the integration without Coriolis forces acting on horizontal velocity perturbations: (a) $t = 75\,000$ s, and (b) $t = 175\,000$ s. Convection is active at both times. See text for energy definitions.

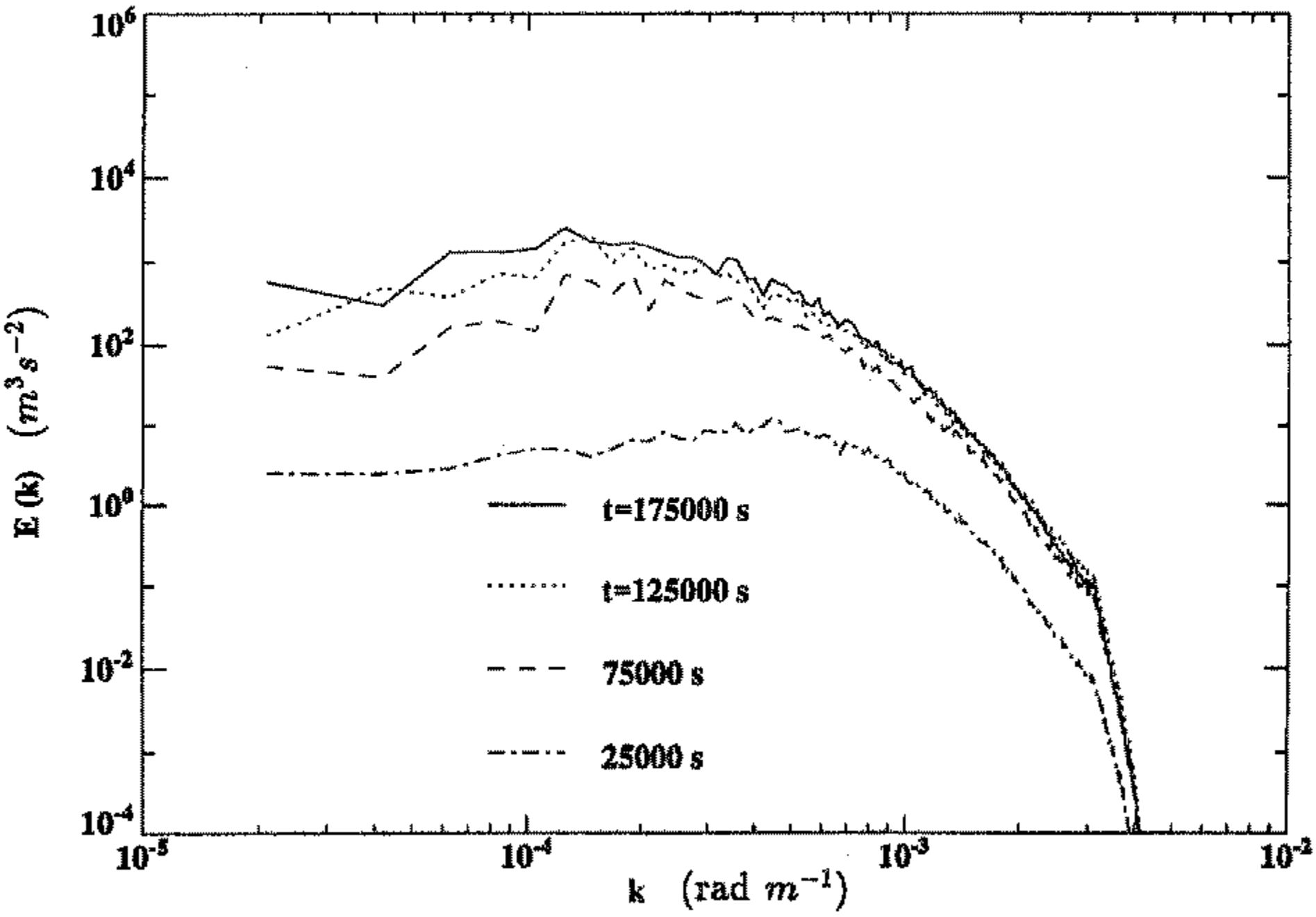

Figure 8. Time evolution of the rotational kinetic energy spectrum in the non-rotating case.

The principal effect of this is to remove mean boundary-layer wind shear thereby denying convection a source of ambient vorticity. As before we consider the form of the convection after about one day of integration. The boundary-layer convective organization is now cellular with cell diameters typically in the range 10–20 km and updraughts concentrated at cell boundaries (Fig. 10(a)). The perturbation potential temperature forms a patchwork of warm and cool regions within the cells, resulting from the cool downdraught's air being deposited at the surface and subsequently warmed (Fig. 10(b)). In mid-troposphere, cellular structure is barely discernible and occurs at a larger scale (though smaller than the control case). The absence of convection lines in this integration is, of course, due to the absence of vertical shear in horizontally averaged wind.

The energy spectra at $t = 175\,000$ s are shown in Fig. 11. In marked contrast to the control integration, and to a greater extent than the $f = 0$ integration, very little rotational energy escapes to scales greater than 30 km. The APE and divergent energy exceed the rotational energy at all scales greater than about 10 km, and by about two orders of magnitude at the largest scales. After a further 100 000 s of integration the rotational energy spectrum still shows little energy in scales greater than 30 km.

Comparing the rotational energy spectrum at $t \sim 175\,000$ s in the current experiment with those of the control and $f = 0$ integrations (Fig. 12), it can be seen that the absence of boundary-layer vertical wind shear has the greatest effect on the creation and upscale propagation of rotational energy. Nevertheless, the earth's rotation also does make an impact on the upscale transfer of energy into horizontal scales of motion greater than 60 km.

(*d*) *'Instant' precipitation*

In 'instant' precipitation integrations, condensed water is removed at each time step and so precipitation-induced downdraughts are unable to form. The main dynamical effect of this is to suppress the counterbalancing of apparent mass sources and sinks caused

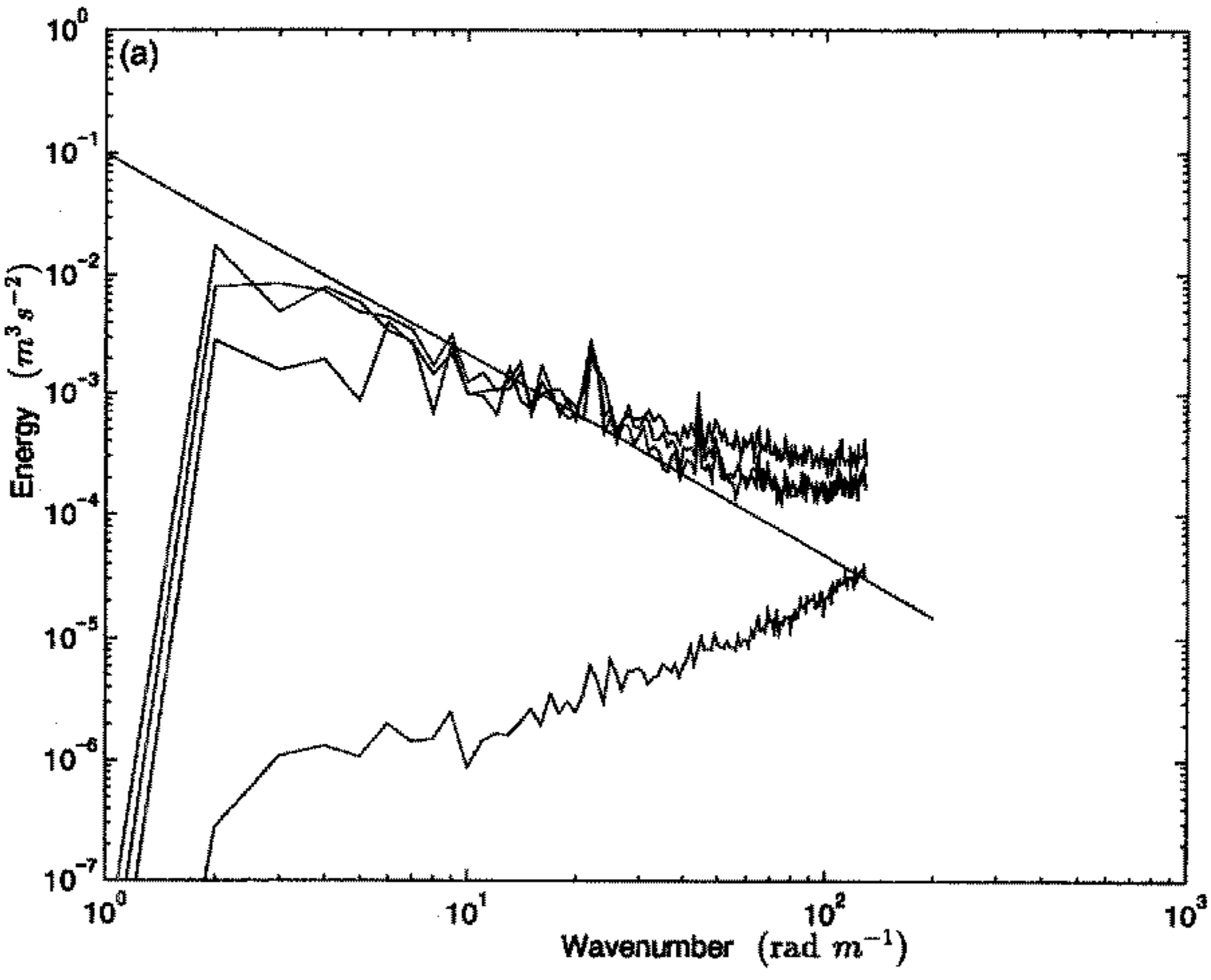

Figure 9. (a) Evolution of the kinetic energy spectrum in a barotropic integration with random, purely dipolar forcing. (b) As for (a), but forcing now has an additional weak monopolar component, of strength 1/100 that of the dipoles. The lowest curve in each panel is the energy spectrum almost immediately after the forcing is turned on, and reflects the spectrum of the forcing. The upper curves show the energy at subsequent times.

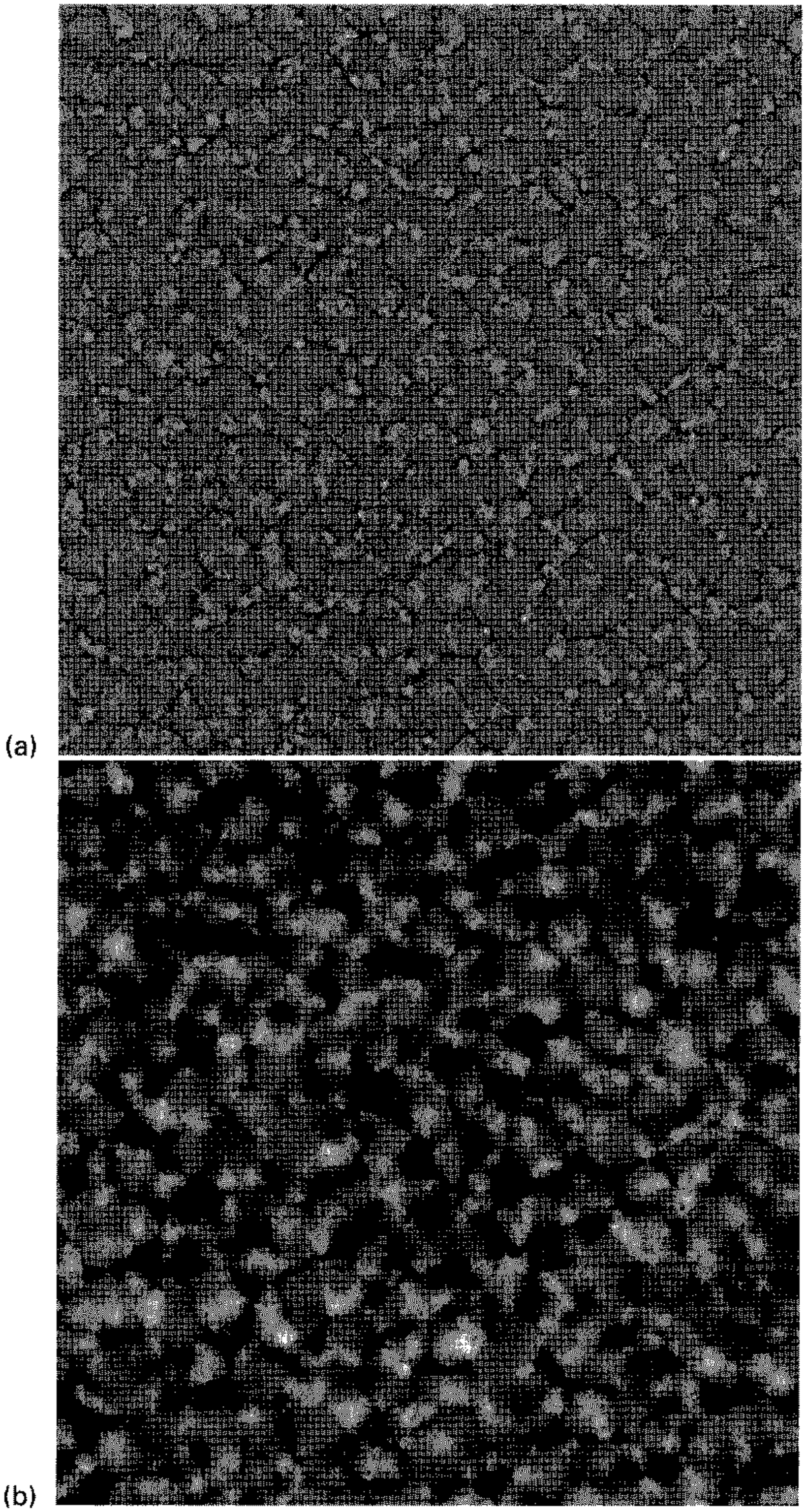

Figure 10. (a) Vertical velocity (range: $-2.7 \rightarrow +3.0$ m s^{-1}) and (b) potential-temperature perturbation (range: $5.2 \rightarrow 7.4$ degC) at $z = 458$ m and $t = 75\,000$ s and where high values are black ($f = 0$ and the horizontally averaged wind is uniform)

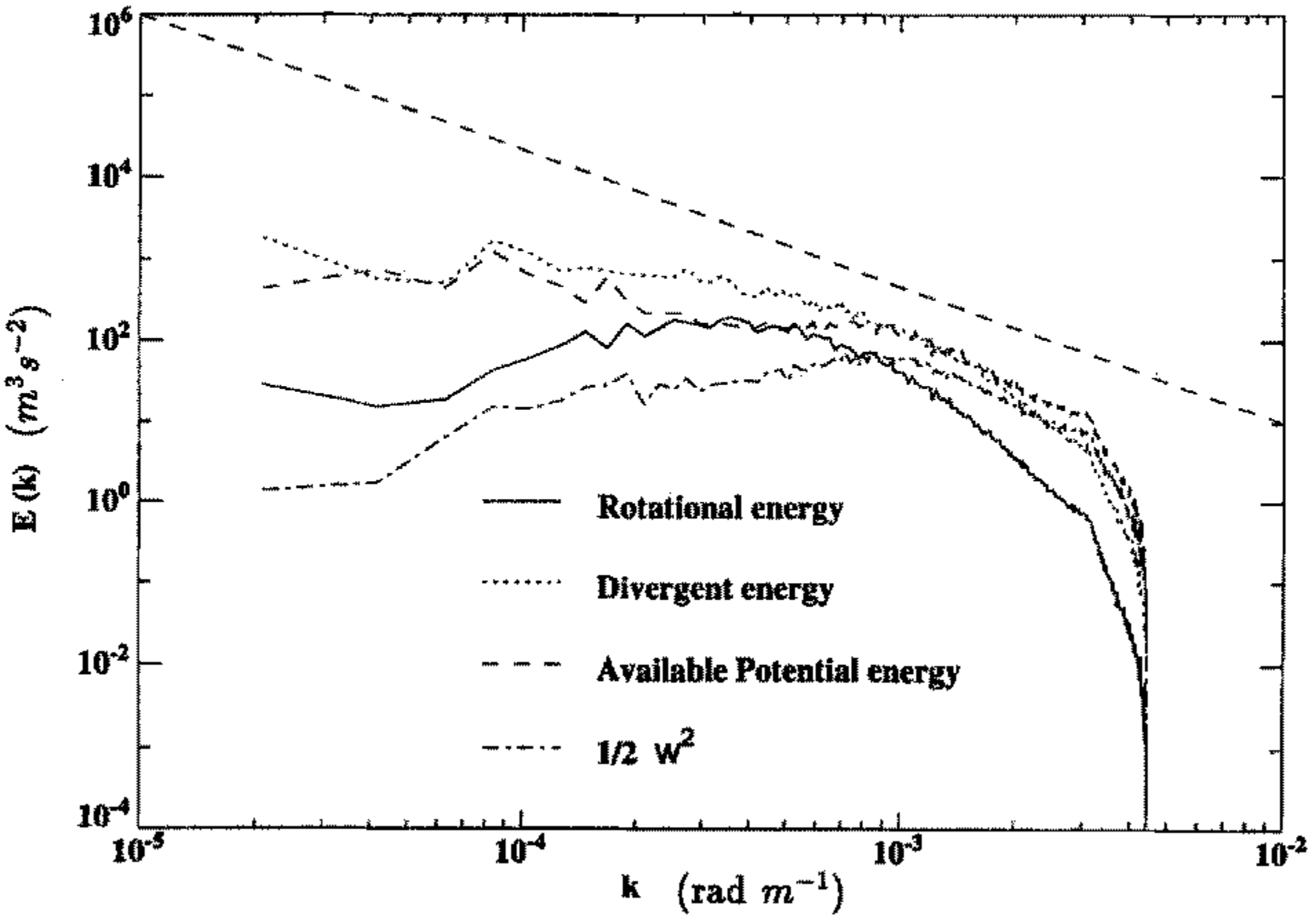

Figure 11. Energy spectra at $z = 7.6$ km, $t = 175\,000$ s (during the active convective phase) when the horizontally averaged wind is uniform and $f = 0$. See text for energy definitions.

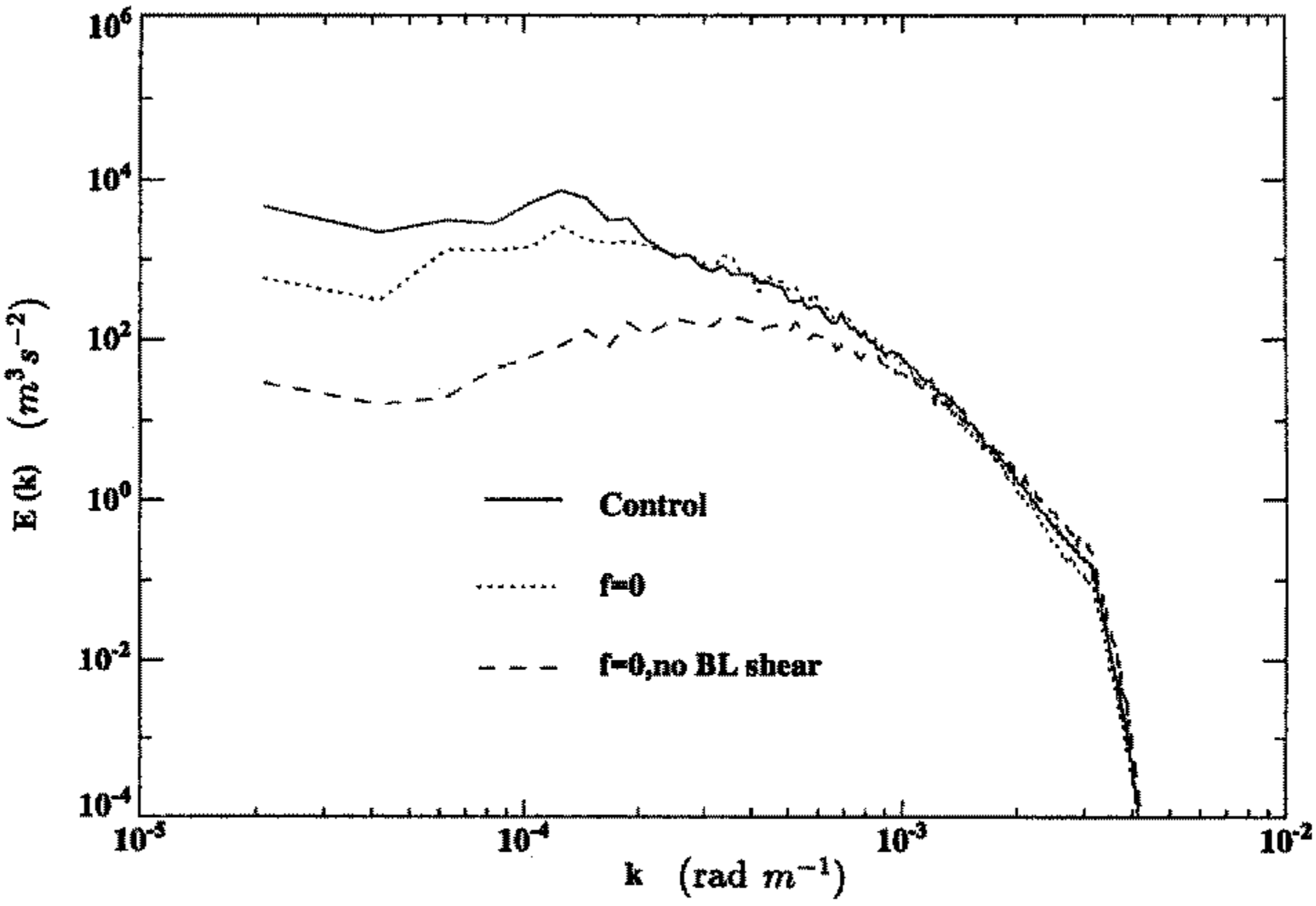

Figure 12. Comparison of the rotational kinetic energy spectra for the control integration with the cases $f = 0$ (on perturbation winds), and $f = 0$ throughout plus uniform horizontally averaged wind at $t \sim 175\,000$ s.

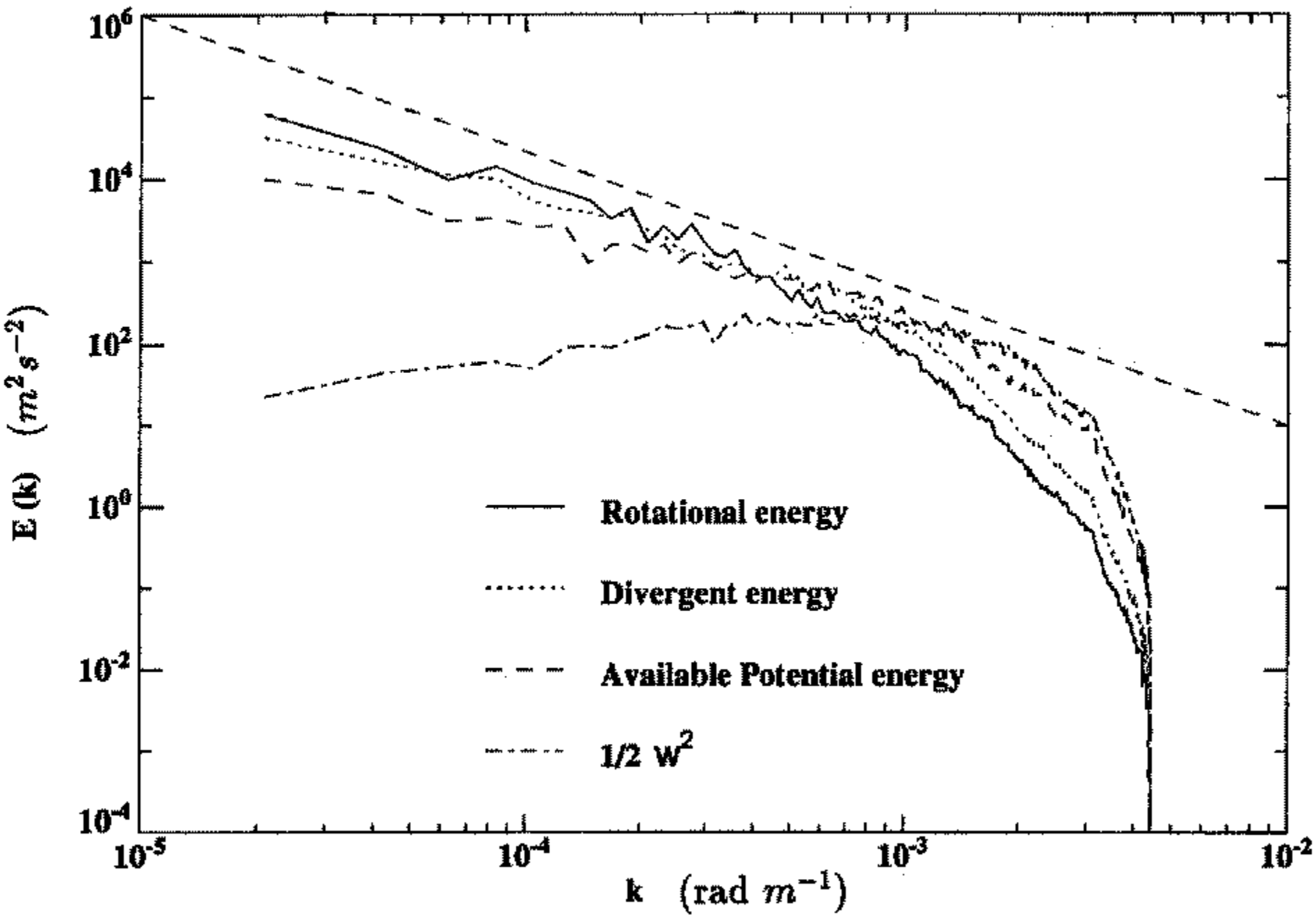

Figure 13. Energy spectra at $z = 7.6$ km, $t = 175\,000$ s for the integration with 'instant precipitation'. See text for energy definitions.

by the downdraught and updraught (respectively) in the lower troposphere. The loss of boundary-layer mass due to convective updraughts then causes local concentration of PV substance and cyclonic spin-up.

The energy spectra at $t = 175\,000$ s are shown in Fig. 13. In this integration there is no local maximum in the rotational energy spectrum, and considerably more rotational and divergent energy is to be found at large scales than in the corresponding case with precipitation. One reason for this is that the absence of precipitation promotes stronger updraughts (due in part to the absence of water loading, as well as the absence of downdraughts) and greater sustained mass transport into the upper troposphere. Also, stronger updraughts in the instant precipitation case are consistent with the higher levels of convective available potential energy (CAPE) that occur: at $t \sim 175\,000$ s the CAPE is ~ 550 J Kg^{-1} compared with ~ 225 J Kg^{-1} in the control integration.

A fascinating aspect of this integration is the clumping of vorticity into three distinct cyclonic cores with diameters of about 10 km. The flow is hurricane-like, yet at a much smaller scale than observed hurricanes. Figure 14 shows an expanded view of the near-surface flow in a 70 km square region enclosing one of these intense mesovortices (potential-temperature perturbation contours are superimposed on wind vectors). The maximum tangential wind speed is 22 m s^{-1} and the centre of the vortex is about 0.5 K warmer than its environment. The vortex extends throughout the depth of the model atmosphere, though with decreasing intensity with height in accordance with hydrostatic and cyclostrophic balance. Emanuel (1989 and personal communication) has suggested that hurricanes may preferentially form where the atmosphere is saturated, so that little evaporation occurs and downdraughts are suppressed; these simulations are consistent with that idea.

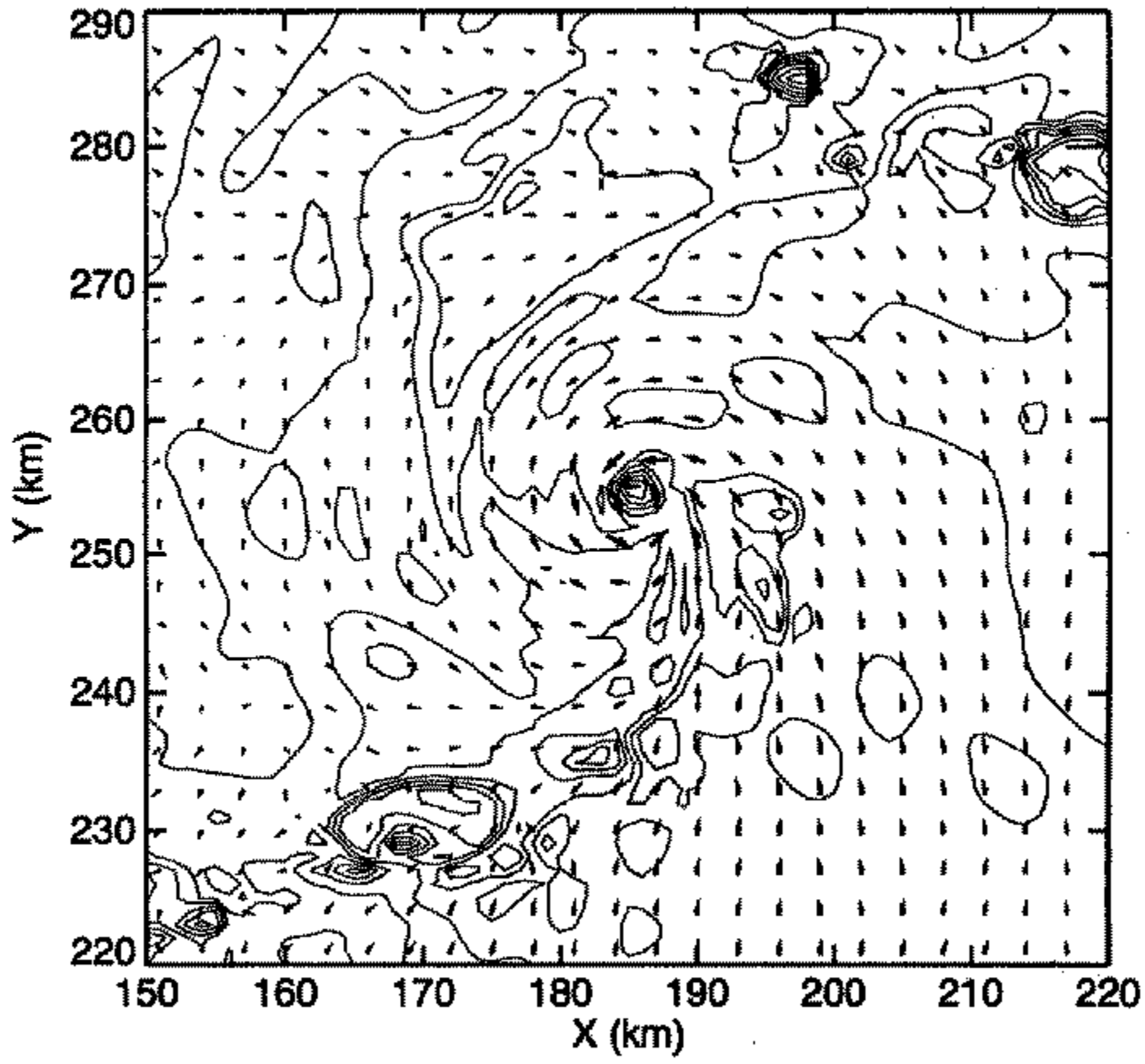

Figure 14. Zoomed region ($\sim 60 \times 60$ km) at time 175 000 s, and at a height 234 m above the surface, showing wind vectors superimposed on the perturbation potential temperature (contour interval: 0.1 K). The centre of the vortex is warmer than the environment by about 0.5 K. The largest wind vector shown corresponds to a wind speed of about 22 m s^{-1}.

(*e*) *Effect of a damping layer*

Finite computational resources dictated the choice of a rigid lid at a height of 10 km. The gravity wave absorbing properties of the stratosphere are thereby lost, and a spurious build-up of gravity wave energy was likely in these experiments. Some additional integrations were therefore performed with a horizontal domain size of 100 km $\times$ 100 km, yet with five extra vertical levels extending up to a height of 18 km in which a stratospheric damping layer was located. Results indicate that this layer reduces divergent energy at large scales, and greatly improves the balance between pressure and velocity, while having much less effect on the inverse energy cascade in the energetic scales.

The stratospheric damping works by relaxing the perturbed prognostic variables back towards their horizontally averaged mean. For an arbitrary prognostic variable, ϕ, this introduces an additional source term of

$$\frac{\partial \phi}{\partial t} = -\lambda\,(z)\left(\phi - \overline{\phi}\right) \tag{12}$$

where λ is the damping coefficient and the overbar denotes the horizontal mean. This is given by

$$\lambda\,(z) = \frac{1}{t_{\mathrm{D}}}\left\{\exp\left(\frac{z - z_{\mathrm{D}}}{H_{\mathrm{D}}}\right) - 1\right\} \tag{13}$$

for $z > z_{\mathrm{D}}$ and equal to zero elsewhere. t_{D} is the damping time-scale and H_{D} a damping height-scale. For the integration presented here $t_{\mathrm{D}} = 1333$ s, $H_{\mathrm{D}} = 5$ km and $z_{\mathrm{D}} = 10$ km. A near-isothermal reference profile is continued for θ into this stratosphere.

The integrations performed with the damping layer are then identical to those without, except for the different geometry and damping layer itself. After 200 000 s the cooling

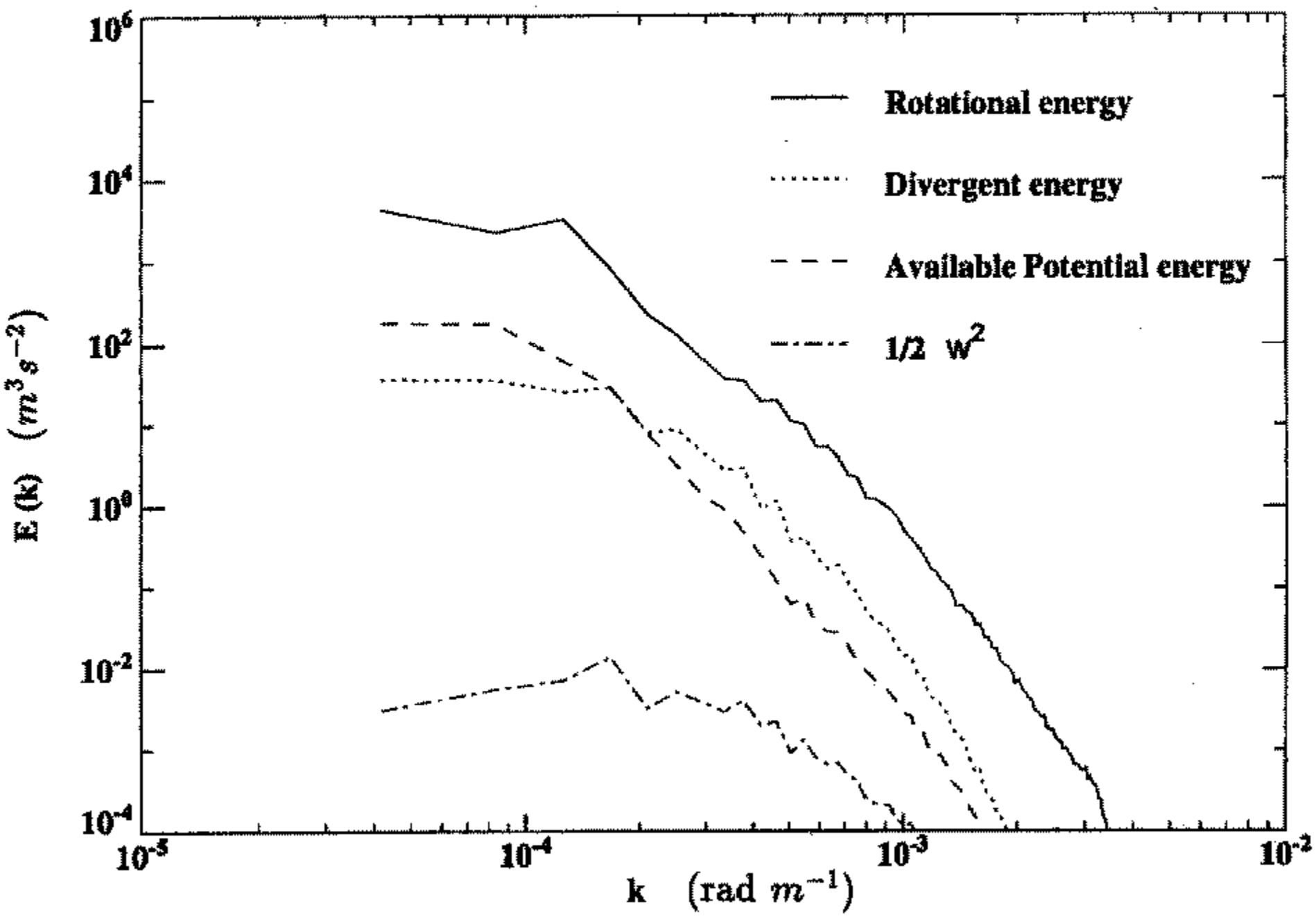

Figure 15. Energy spectra at $z = 7.6$ km, $t = 300\,000$ s for the reduced horizontal domain with damping layer. This is 100 000 s into the decay phase of the simulation. See text for energy definitions.

function and surface energy fluxes were switched off and the integration continued for another 100 000 s. Figure 15 shows the energy spectra at $t = 300\,000$ s. Comparing these spectra with those of the control integration at the same time (Fig. 6) it is clear that the kinetic energy in vertical motion is reduced by over two orders of magnitude, indicating that the damping layer has successfully absorbed gravity waves. There has also been a marked reduction in divergent kinetic energy at the largest scales in the domain and similarly in APE at most scales. On the other hand, the rotational energy has a similar magnitude to the control integration at scales greater than 30 km, but is reduced at smaller scales.

4. Diagnosis of balanced motion

(*a*) *Potential-vorticity inversion: formulation*

Identification of balanced motion simply as the rotational part of the wind in a level surface is not of course exact. For example, vortex lines generated by baroclinic forces lie within isentropic surfaces and these surfaces are not precisely horizontal, so the intersection of vortex lines with level surfaces will appear as rotational energy. Thus we seek a slightly more general definition of balance, and investigate the extent to which rotational energy is, in fact, a useful proxy.

Balanced flow, almost by definition, satisfies some diagnostic balance between velocity and pressure. A more general definition would be that all dynamical fields can be diagnosed from knowledge of a non-trivial subset. Although geostrophic balance is the best known, balanced motion exists in various other circumstances, such as low Froude number flow (Lilly 1983; McWilliams 1985). In geophysical flows, balance is typically characterized by the interior evolution of a single 'prognostic' variable, with the other variables following from 'invertibility' relationships. Using PV rather than some other

field (say pressure) as the fundamental inversion variable is advantageous from both the dynamical and practical points of view (Davis and Emanuel 1991; Vallis 1996). Regarding the former, we note that PV is a purely advected quantity in the absence of diabatic or frictional forcing, and its evolution, in the linear approximation, is unaffected by gravity wave propagation. An inversion based on, say, pressure might lead to the mistaken diagnosis of gravity waves as balanced motion. And although potential temperature is also purely an advected field, its contribution may be considered to be in providing vertical boundary conditions for the PV inversion, through its lateral advection at these boundaries. From a practical perspective, we see below that PV inversion can be achieved (to the accuracy of the scaling producing the inversion) simply by the solution of linear elliptic equations, at least in the low Froude number or low Rossby number limit.

For low Froude number flow an approximation to the PV valid for all Rossby numbers is given by (Vallis 1996):

$$Q \approx f\widehat{\theta}_z + \widehat{\theta}_z \nabla_h^2 \psi + f\theta'_z. \tag{14}$$

where $\widehat{\theta}$ is the mean and θ' the perturbation potential temperature, ψ the horizontal-velocity stream function, and ∇_h^2 is the two-dimensional (horizontal) Laplacian. The inversion is closed using gradient-wind balance,

$$\nabla_h^2 \frac{p'}{\widehat{\rho}} - f\nabla_h^2 \psi = 2J(\psi_x, \psi_y), \tag{15}$$

which gives a relationship between pressure and velocity, and hydrostatic balance,

$$g\frac{\theta'}{\widehat{\theta}} = \frac{\partial}{\partial z}\left(\frac{p'}{\widehat{\rho}}\right). \tag{16}$$

Combining these into a single formula for stream function gives

$$Q = f\widehat{\theta}_z + \widehat{\theta}_z \nabla_h^2 \psi + \frac{f}{g}\frac{\partial}{\partial z}[\widehat{\theta}\{f\psi_z + \nabla_h^{-2} J_z(\psi_x, \psi_y)\}]. \tag{17}$$

Here, ∇_h^{-2} is a symbolic notation for the solution of the two-dimensional Poisson problem. Aside from the Jacobian term, this is a linear inversion, very similar to the standard quasi-geostrophic formula for PV in terms of stream function. The Jacobian term may in fact be ignored if either the Froude or Rossby number is sufficiently small, which is of course the criterion for the balanced motion to exist. If the Rossby number is small the Jacobian is small, because it is a small correction in (15) and geostrophic balance is presumed to hold. Then, to the accuracy of the scaling, the inversion is:

$$Q \approx f\widehat{\theta}_z + \widehat{\theta}_z \nabla_h^2 \psi + \frac{f}{g}\frac{\partial}{\partial z}\left(\widehat{\theta} f \psi_z\right). \tag{18}$$

The third term on the right-hand side will be sufficiently small as to be negligible in many circumstances, plainly including the $f = 0$ case. The magnitude of the third term relative to the second term on the right-hand side is $(Fr)^2/(Ro)^2$ under a scaling from geostrophic balance, and is $(Fr)^2/(Ro)$ under a small Froude number scaling (Vallis 1996). Thus, if the flow is sufficiently stratified the third term is small, whereas a small Rossby number tends to increase the importance of the stratification term. Equivalently, the stratification term will be small if the available potential energy of the flow is much

smaller than its horizontal kinetic energy, a criterion which was seen to hold reasonably well in our analyses, even in the rotating cases. In these cases, the inversion (18) reduces to the simple formula

$$Q \approx \widehat{\theta}(f + \nabla_h^2 \psi) \tag{19}$$

where $f = 0$ if there is no background rotation. The gradient wind balance (15) then reduces to the purely cyclostrophic balance $\nabla_h^2(p'/\widehat{\rho}) = 2J(\psi_x, \psi_y)$.

The above formulae for PV inversion involve only the solution of linear elliptic equations. This is the practical advantage of a PV inversion. The gradient wind may of course be important in subsequently determining the pressure and temperature from the velocity field using (15) and (16), but again these are linear formulae.

Equation (17) requires a boundary condition at the top and bottom. A Neumann condition (specifying ψ_z) is natural, this implying a temperature specification in the low Rossby number limit. In the general case the (nonlinear) boundary condition is

$$\psi_z = \frac{g}{f}\frac{\theta'}{\widehat{\theta}} - \frac{2}{f}\nabla_h^{-2}\left\{J_z(\psi_x, \psi_y)\right\}. \tag{20}$$

Even though the Jacobian term may be large in this equation, its contribution to the interior solution is always small; in the low Rossby number case the term itself is small, and in the low Froude number case the high stratification prevents the vertical propagation of boundary influences. Thus, as with the interior equation (18), scaling reveals that the Jacobian term may again be ignored.

(*b*) *Results*

The simulations with a damping stratosphere generally show a much better balance between pressure and velocity than the rigid-lid simulations, although the dominance of rotational over divergent energy, and the inverse cascade of rotational energy to large scales, are similar with and without the model stratosphere. We shall show inversions in both the active convective phase of the integrations, and in the decay phase after the surface fluxes have died away, for integrations both with and without background rotation. For each we show two types of result: a velocity inversion from the model PV field, and a diagnosis of the pressure field from the velocity field. The former is primarily an illustration of the dominance (or otherwise) of the rotational component of the velocity field, whereas the latter is a direct indication of balance between pressure and velocity. Given the diagnosis of the pressure field via a balance relationship, the temperature field can then be deduced using hydrostatic balance (except in strong updraughts and other regions of violent acceleration where hydrostatic balance is not a good approximation). Note that inverting for the velocity field is a more severe test than inverting for the vorticity field since, given relatively flat isentropes which do not depart too much from the basic state, obtaining the vorticity from the PV is largely a matter of division and subtraction.

The same inversion formulae can be used in all cases, with or without rotation. Specifically, (18) yields the stream function, and the velocity is obtained from it by a single differentiation. The pressure may then be diagnosed from the velocity using:

$$\nabla_h^2 \frac{p'}{\rho_0} = f_0 \nabla_h^2 \psi + 2J(u, v). \tag{21}$$

Note that the cyclostrophic (Jacobian) term cannot be neglected in this equation if the Rossby number is O(1) or larger, because it is then at least the same order of magnitude as the other terms. However, the Jacobian term *is* small in (17)—see Vallis (1996).

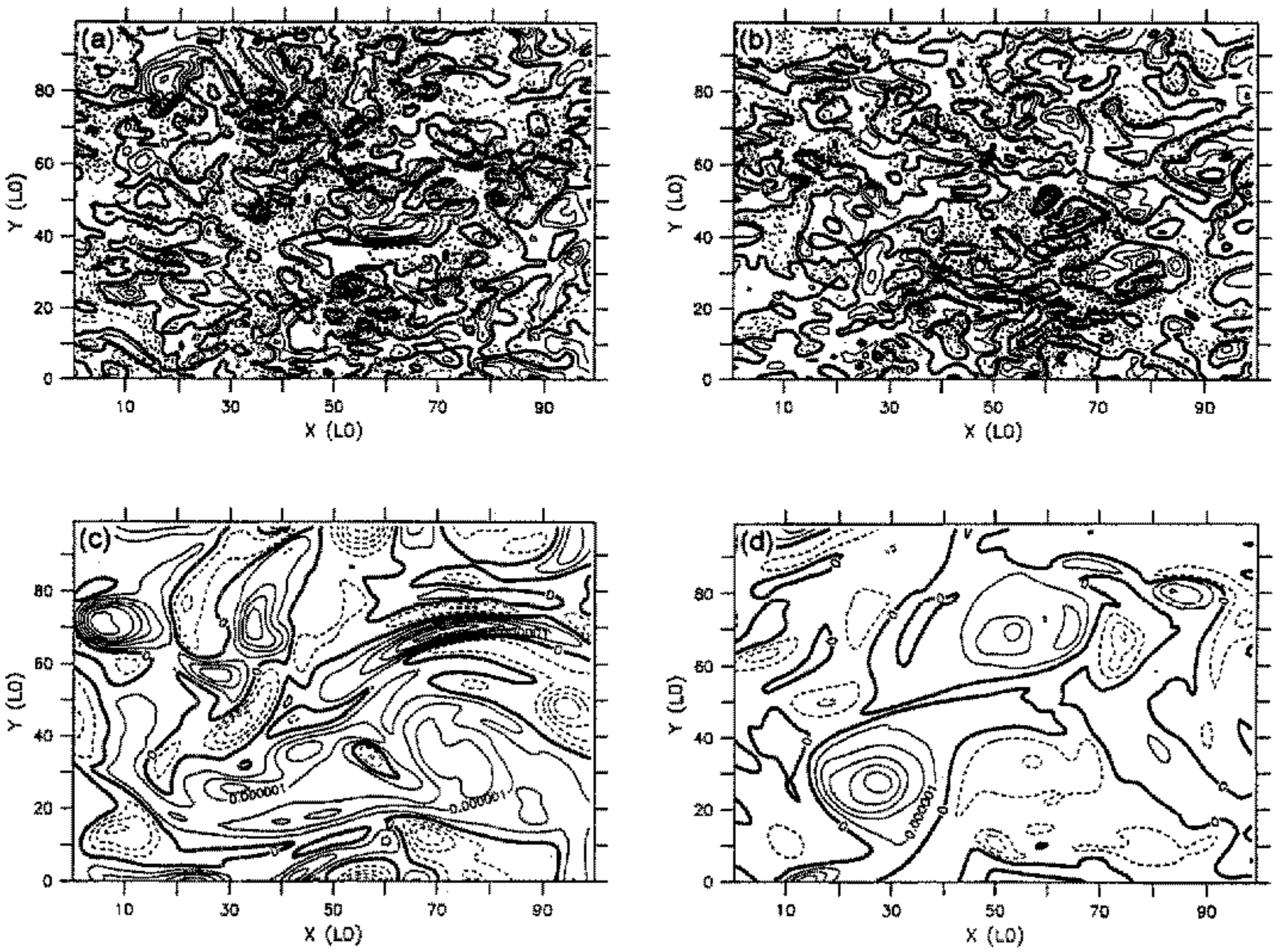

Figure 16. Potential-vorticity field at 7.6 km for various integrations. (a) Rotating, active convection; (b) non-rotating, active convection; (c) non-rotating, decay phase; and (d) rotating, decay phase. See text for further explanation.

Figure 17 shows velocity and vorticity inversions, obtained from the PV field illustrated in Fig. 16 (upper left panel). Clearly, the features at a scale larger than about 10 km are reproduced by the inversion, but the smaller-scale features, especially those in the vicinity of active convection are not. The inversion for the rotating case is perhaps slightly better than that for the non-rotating case, indicative of the greater dominance of rotational energy, although the difference is not marked. In the decaying phase of the integrations, after the cessation of active convection, the accuracy of the inversions further improves (Fig. 18). During this period the energy associated with divergent velocity is decaying, and the rotational energy is being transferred to larger scales as indicated by the much larger scale of the structures in Fig. 16.

Two other points are worth making. Firstly, the inversions shown are technically fully 'three-dimensional,' in that they solve the three-dimensional elliptic equation (18). (The method of solution is to project the vertical structure onto eigenmodes of the operator $\partial/\partial z(\widehat{\theta}\partial/\partial z)$, using the same vertical grid as is used in the model integrations. This results in a set of two-dimensional Poisson equations for each vertical mode, which can be solved by standard methods, from which the vertical structure in physical space is reconstructed.) Inversions obtained by neglecting the third term on the right-hand side of (18) (i.e. two-dimensional inversions) were also obtained, and these proved to be very similar to those obtained using the full three-dimensional equation. (Note that this term is only present in the case with rotation.) This is consistent with the smallness of the available potential

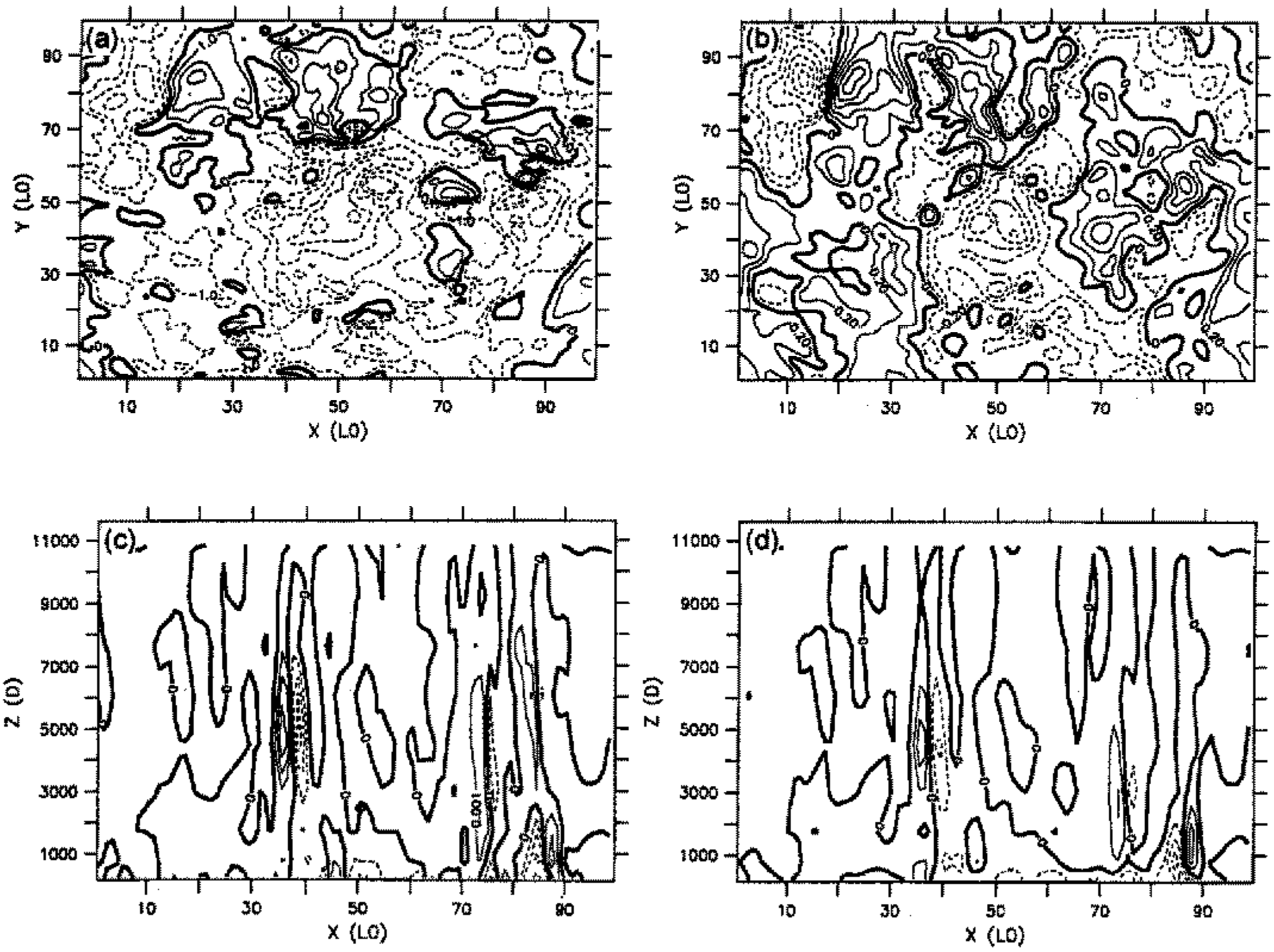

Figure 17. Velocity and vorticity inversions from the integration with rotation and a wave-damping stratosphere, at a time $t = 200\,000$ s, during the active phase of convection. (a) Meridional velocity at 7.6 km, (b) inverted velocity field obtained using (18), (c) a vorticity section in the zonal plane across the domain, and (d) inverted vorticity field.

energy compared with the kinetic energy, and with the Froude number being very small (~ 0.03). Secondly, note that in the decaying phase of the integrations the vertical scale of the vorticity field *diminishes*. This is counter to the expectation of the inverse cascade in geostrophic turbulence, in which the system seeks the gravest mode, both horizontally and vertically. Rather, it is indicative of stratified turbulence; if each layer is largely uncoupled from its neighbours, the layers will evolve more or less independently of each other, and the vertical scale will therefore, in general, diminish. In the cases with rotation, the stiffening effect of background rotation is evidently insufficient to prevent this.

Examination of the balance between velocity and pressure reveals a similar picture. Figures 19 and 20 show the actual pressure field and the pressure field 'inverted' from the velocity field, using various forms of geostrophic and gradient-wind balance. Even in the active phase of the convection, there is a reasonable balance between pressure and velocity for features of scale greater than 20 km (Fig. 19). This balance exists in both the rotating and non-rotating cases, with slightly better agreement being obtained in the former. After the cessation of active convection, the balance becomes almost perfect (Fig. 20). Note that in the cases with rotation, both the effect of geostrophic balance ($\nabla^2 p' \sim \widehat{\rho} f_0 \zeta$) and cyclostrophic balance ($\nabla^2 p' \sim 2\widehat{\rho} J(u, v)$) contribute to the balance, in approximately equal measure. In cases without rotation, cyclostrophic balance alone is achieved.

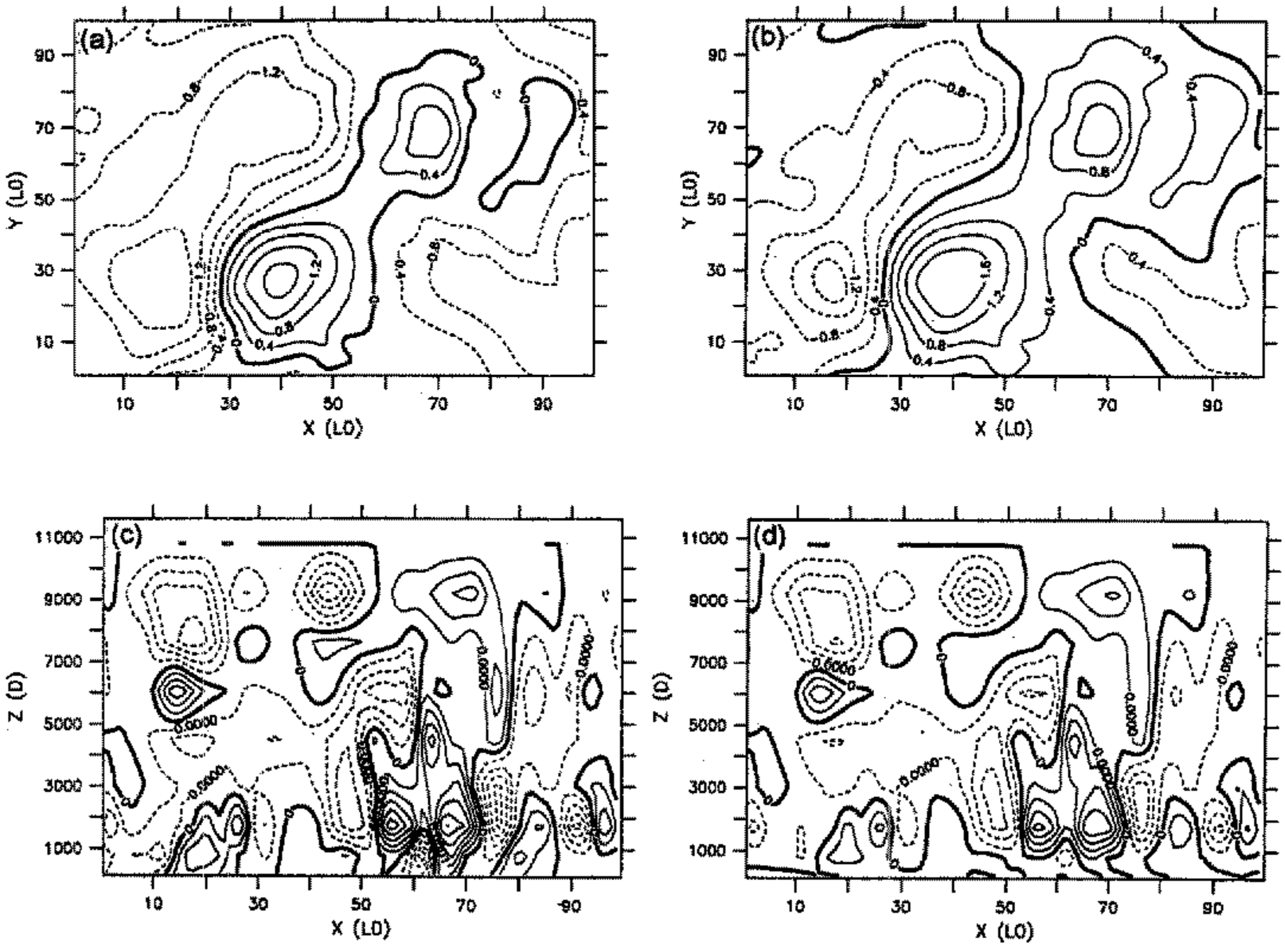

Figure 18. As Fig. 17, but at a time 100 000 s into the decay phase of the integrations.

5. Discussion

Three-dimensional convectively resolving simulations are, naturally enough, computationally demanding and this necessitates some compromises. Some of the integrations chosen here may be considered rather extreme as far as a realistic mesoscale simulation is concerned, for example in having no boundary-layer shear or no cloud/precipitation. At the same time, the model is rather complex compared with (and certainly more similar to the real atmosphere than) simpler geophysical fluid dynamics models often used to simulate stratified turbulence. These are typically 'dry' and Boussinesq, as opposed to the moist quasi-Boussinesq/anelastic model used here. Using such models one is able to control the nature of the forcing more closely. For example, Herring and Métais (1989) were able to use a narrow spectral band forcing, whereas the naturally occurring convection in our simulations will, even though it is at small scale, have a broader spectral signature. The compromise we have chosen hopefully gives insight into important physical mechanisms, but at the same time is realistic enough to be of direct relevance to the atmospheric mesoscale.

Stratified turbulence at scales larger than the convection arises from forcing by potential-vorticity anomalies, which can persist after convection has ceased. There are three sources of vorticity that need to be considered: ambient background rotation associated with the Coriolis parameter, horizontal vorticity associated with boundary-layer wind shear, and baroclinic generation of vorticity in the interior due to horizontally varying buoyancy forces. The first two are more important and active in our integrations; the third

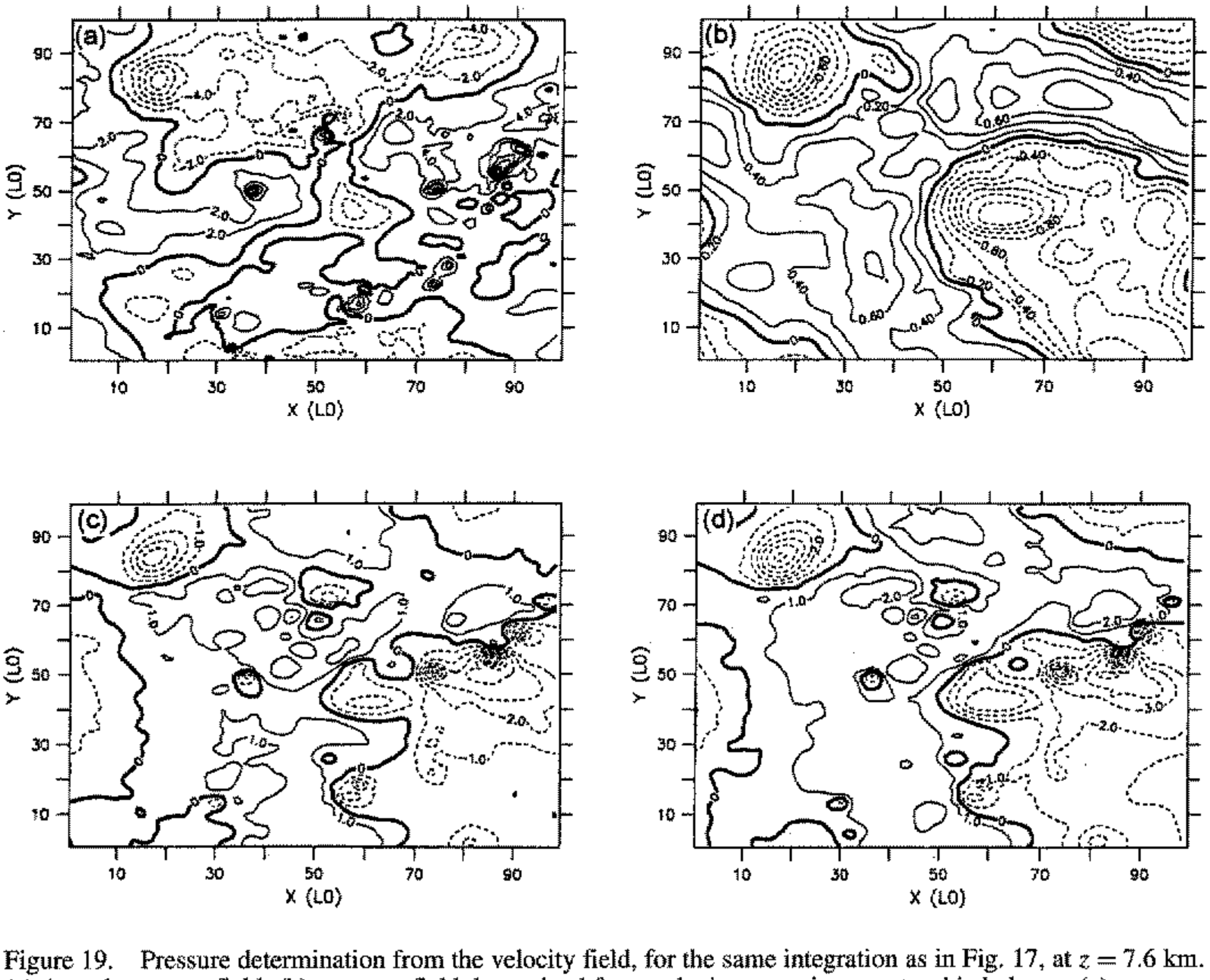

Figure 19. Pressure determination from the velocity field, for the same integration as in Fig. 17, at $z = 7.6$ km. (a) Actual pressure field; (b) pressure field determined from velocity assuming geostrophic balance; (c) pressure field determined from velocity using cyclostrophic balance only (i.e. $\nabla^2(p/\widehat{\rho}) = 2J(u, v)$); and (d) pressure field determined from sum of (b) and (c), that is using Eq. (15).

mechanism is associated with buoyant convective updraughts which can create toroidal vortex lines. In some situations this horizontal vorticity may be tilted into the vertical, as in the squall-line simulations of Davis and Weisman (1994). Their convective systems cover a much large area than our simulations, with updraughts sloping 50 km in the horizontal over the depth of the troposphere. In our simulations the updraughts are essentially vertical. This difference in the structure of the convection must, in part, be due to their deep (lowest 2.5 km) shear layer compared with the shallow boundary-layer wind shear in the simulations presented here. Of the mechanisms forcing vertical vorticity in their simulations, the dominating one is the tilting of horizontal vorticity generated by buoyancy forces at the sloping updraught–downdraught boundary—particularly at the ends of the squall line. We believe that the absence of squall-line structure in our simulations greatly reduces the effectiveness of this vorticity-forcing mechanism.

The principal source of vertical vorticity in our simulations comes mainly from the twisting of horizontal vorticity filaments from the frictional boundary layer by deep convective updraughts. Such arguments are difficult to put on a rigorous footing, since vortex lines are not carried with the flow in a stratified fluid. However, it is clear from the integration with fixed horizontally averaged wind that, in that case, an important source of enstrophy had been removed. The concentration of ambient PV in the rotating simulations provides in addition an important monopolar component to the vorticity forcing.

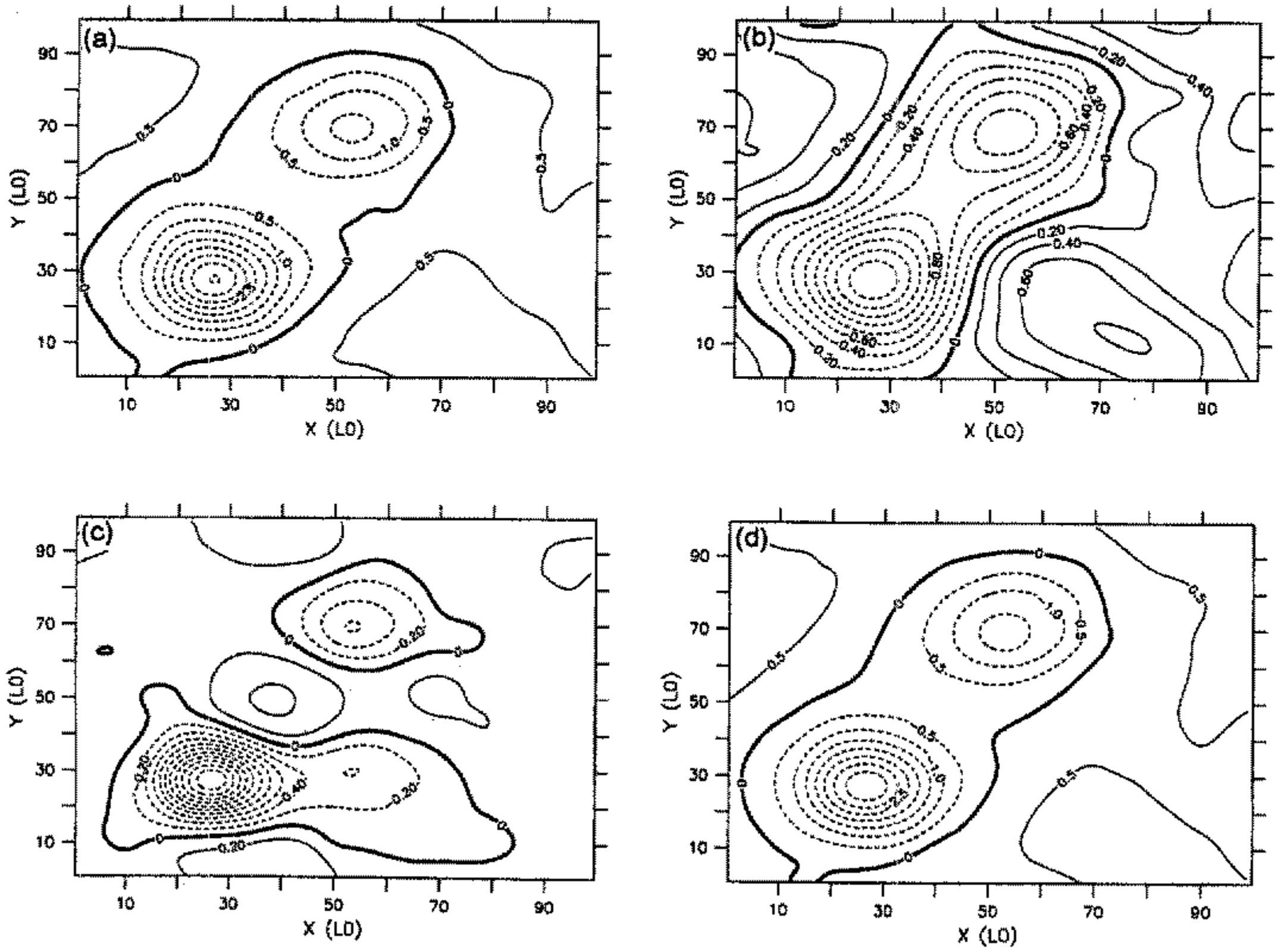

Figure 20. As Fig. 19, but at a time 100 000 s into the decay phase of the integration.

'Two-dimensionalization' of a flow can arise, in general, in two circumstances—highly stratified (low Froude number) flow or rapidly rotating (low Rossby number) flow, or a combination of both. In the rotating case, the lowest order inversion of PV is essentially given by quasi-geostrophic relationships—the rotation imparting some vertical stiffness to the flow. However, high stratification opposes this and acts to decouple layers in the vertical. In the simulations presented here, the horizontal layers are effectively decoupled in the vertical; a 'quasi-geostrophic' inversion using (18) to obtain the velocities is little improvement over the simple two-dimensional inversion (19). It is then a reasonable approximation to simply equate 'balanced energy' with the kinetic energy of the rotational wind.

Upscale energy transfer is found to occur in the integrations both with and without background rotation. The quasi-horizontal nature of the flow is further enhanced in the spin-down phase of the integrations after the active convection subsides. This phase is marked by a dominance of rotational energy over divergent energy, and a selective decay of enstrophy over energy, both characteristic features of quasi-horizontal flow. In cases with a wave-damping stratosphere, a very good balance between pressure and velocity is achieved, characteristic of quasi-horizontal balanced flow.

There are nevertheless differences in the rotating and non-rotating simulations. For example, in the rotating simulation, the vorticity field assumed a different character after one day of integration, with the appearance of large-scale features. Energy spectra showed that for scales greater than about 60 km there was an order of magnitude more rotational kinetic energy in the integration with Coriolis force. The precise mechanism for this en-

hanced large-scale energy with rotation is not clear. One possibility is that the monopolar PV forcing in the upper troposphere in the rotating case greatly enhances the long-range influence of the forcing, thereby assisting the upscale transfer of energy. In contrast, the dipolar and quadrapolar PV fields forced by vortex twisting produce compact horizontal circulations with only short-range influence. Thus, although stratified two-dimensional turbulence is produced in the integrations both with and without rotation, the rate of the upscale energy transfer is greatly enhanced by the nature of the forcing in the former case.

The production of balanced flow and non-negligible upscale energy transfer in the non-rotating case is in some contrast to earlier simulations by Herring and Métais (1989), although a direct comparison is difficult because of the very different types of simulation. The 'two-dimensionalization' of the flow, especially in the decay phase, plainly does take place even in the absence of rotation in our simulations. One difference between our results and the earlier ones is that the Froude number in our simulations is very small, typically $\ll 0.1$, whereas in their simulations it is ~ 0.2, and is perhaps unable to produce sufficient two-dimensionalization without the additional help of background rotation. Note that the limit of highly stratified flow is highly layered flow, which may lead to shearing instabilities and/or large frictional effects, either of which may inhibit the inverse cascade. Strong rotation, accompanied by low Rossby number, will inhibit vertical motion and strengthen the vertical coherence of the flow, thereby resisting the tendency towards layering and dissipation. By using a large-eddy model with limited vertical resolution, our flows are less viscous and at the same time do not allow very small vertical scales to develop, which allows the Froude number to remain small. (Bartello (1995) further discusses the effect of rotation on highly stratified flow.) A possible interpretation of our study is that the quasi-horizontal limit of highly stratified flow can be achieved and is evidently stable. However, the evolution of stratified turbulence in the model is constrained by coarse vertical resolution, which allows the Froude number to remain low and the Richardson number high. The inability of the model to permit vertical fine-structure (and accompanying turbulent dissipation) thus prevents us from drawing general conclusions about the realizability of quasi-horizontal flow in stratified turbulence.

The apparent observation of the spectrum becoming shallower in the mesoscale to one close to $k^{-5/3}$ is nevertheless not fully explained by these simulations. Although in the regime of active forcing a spectrum close to $-5/3$ is produced by the model, in the spin-down phase the spectrum steepens as enstrophy is dissipated. Also, the observations themselves are likely to be somewhat biased away from regions of active convection. Seen in this light it is perhaps surprising that the observed spectra fit the classical $-5/3$ inverse cascade spectrum so well.

The impact of instant precipitation was quantitatively large in our integrations, with the formation of several intense 'meso-cyclones' with warm core structure. The effective mass source/sink dipole due to convection is enhanced in this situation since a convective downdraught is not formed. The degree to which convective-scale downdraughts form may well be germane to the problem of tropical storm initiation. If environmental conditions (or convective storm organization) favour weak downdraughts over tropical oceans then the spin-up of a low-level cyclone would provide the necessary 'seed' to assist moisture convergence. The presence of a damping 'stratosphere' also had a quantitatively large effect in that it evidently aids the adjustment process by allowing gravity waves to be efficiently damped, resulting in a greater degree of balance (geostrophic plus cyclostrophic) between pressure and velocity.

If an upscale energy transfer can be produced in the atmospheric mesoscale, what are the implications for synoptic and larger-scale flow? Here the answers are less clear. The importance is plainly dependent on the rate at which balanced kinetic energy, generated by

deep convection, is transferred to synoptic and mesoscales. To estimate this, we computed the rotational energy in scales greater than 60 km as a function of time, and thereby estimated its tendency. Since dissipation in these scales is likely to be small, the upscale energy transfer rate must be of similar magnitude. In the last day of the reference integration (with rotation and precipitation), this rotational energy tendency was found to be about 0.1 m^2s^{-2} per day; when the Coriolis parameter was set to zero, however, this fell to 0.05 m^2s^{-2} per day. In contrast, the integration with rotation and 'instant precipitation' had an estimated rotational energy tendency of about 1 m^2s^{-2} per day, largely through the production of intense vortices. This last figure is comparable with the estimate of energy injection rate given by Lilly (1983) based on fitting a $k^{-5/3}$ inertial sub-range energy spectrum to observed data, using the inertial range formula

$$E(k) = \mathcal{K}\epsilon^{2/3}k^{-5/3} \tag{22}$$

where $\mathcal{K}$ is the Kolomogorov constant and ϵ the energy transfer rate. Typical estimates of $\mathcal{K}$ range from 6 to 9, and using 7, Lilly estimates $\epsilon = 10^{-5}$ m^2s^{-3}. Evidently, the balanced energy tendency in our integrations is smaller than this estimate.

It is probably unlikely, even with Lilly's higher estimate of cascade rates, that the *direct* effects of the upscale energy transfer are significant in organizing large-scale flow. The efficiency with which convectively generated kinetic energy is captured in quasi-two-dimensional balanced motion, and then cascaded upscale, is relatively small unless organized into MCSs. This, in itself, is not entirely unexpected given the earlier studies of Schubert *et al.* (1980) and Shutts and Gray (1994) but does place their inferences on a firmer footing through direct numerical simulation.

There may nevertheless be important consequences for numerical weather prediction. The production of upscale kinetic energy transfer is likely to be an important limitation on atmospheric flow predictability. The growth of error in such a regime is likely to be much faster than in a downscale enstrophy cascading regime, for two reasons. First, the energy spectrum is much more shallow and therefore relatively more energetic at small, ill-observed scales; the growth of error can be expected to be roughly proportional to the eddy-turnover time (Leith and Kraichnan 1972; Vallis 1985), and therefore tends to be faster in a shallower spectrum which has more energy at small scales. Second, if energy itself is being cascaded to large scales then the error transfer is in the same (spectral) direction, and hence is likely to be more rapid than an upscale error transfer in a forward cascading region. The upshot of these considerations is that the predictability time in the mesoscale is likely to be of the order of one-to-a-few eddy-turnover times, rather than being several times the eddy-turnover time. Using a velocity of 2 m s^{-1} gives an estimate of an eddy-turnover time, and hence a theoretical predictability time, at a scale of 300 km to be of order 1.5×10^5 seconds, or about 2 days. Errors at this scale will subsequently propagate to the large scale, giving estimates of the large-scale predictability time of several days—perhaps somewhat smaller than traditional theoretical estimates based on a continuing forward enstrophy cascade into the mesoscale. Nonetheless, the statements made in this paragraph should be regarded as speculation.

Acknowledgements

We would like to thank Paul Mason who provided much of the initial motivation for this project, Chris Snyder whose thorough reading of the paper led to a much-improved revised version, Doug Lilly and Wayne Schubert for enlightening discussions and/or comments, and the National Science Foundation for providing support to the first author under grant number ATM 93-17485.

References

Bartello, P. 1995 Geostrophic adjustment and inverse cascades in rotating stratified turbulence. *J. Atmos. Sci.*, **52,** 4410–4428

Boer, G. J. and Shepherd T. G. 1983 Large-scale two-dimensional turbulence in the atmosphere. *J. Atmos. Sci.*, **40,** 164–184

Charney, J. G. 1971 Geostrophic turbulence. *J. Atmos. Sci.*, **28,** 1087–1095

Davis, C. A. and Emanuel, K. A. 1991 Potential vorticity diagnosis of cyclogenesis. *Mon. Weather Rev.*, **119,** 1929–1953

Davis, C. A. and Weisman, M. L. 1994 Balanced dynamics of mesoscale vortices produced in simulated convective systems. *J. Atmos. Sci.*, **51,** 2005–2030

Emanuel, K. A. 1989 The finite amplitude nature of tropical cyclogenesis. *J. Atmos. Sci.*, **46,** 3431–3456

Gage, K. S. and Nastrom, G. D. 1986 Theoretical interpretation of atmospheric wavenumber spectra of wind and temperature observed by commercial aircraft during GASP. *J. Atmos. Sci.*, **43,** 729–739

Gray, M. E. B. 1996 'Geostrophic adjustment following deep convection'. PhD thesis, University of Reading

Haynes, P. H. and McIntyre, M. E. 1990 On the conservation and impermeability theorems for potential vorticity. *J. Atmos. Sci.*, **47,** 2021–2031

Herring, J. and Métais, O. 1989 Numerical experiments in forced stably stratified turbulence. *J. Fluid Mech.*, **220,** 97–115

Kessler, E. 1974 Model precipitation and vertical air currents. *Tellus*, **26,** 519–542

Leith, C. E. and Kraichnan, R. H. 1972 Predictability of turbulent flows. *J. Atmos. Sci.*, **29,** 1041–1058

Leonard, B. P. 1991 The ULTIMATE conservative difference scheme applied to unsteady one-dimensional advection. *Comput. Methods Appl. Mech. Eng.*, **19,** 17–74

Lilly, D. K. 1983 Stratified turbulence and the mesoscale variability of the atmosphere. *J. Atmos. Sci.*, **40,** 749–761

1989 Two-dimensional turbulence generated by energy sources at two scales. *J. Atmos. Sci.*, **46,** 2026–2030

McWilliams, J. C. 1985 A uniformly valid model spanning the regimes of geostrophic and isotropic stratified turbulence. *J. Atmos. Sci.*, **42,** 1773–1774

Maltrud, M. E. and Vallis, G. K. 1991 Energy spectra and coherent structures in forced two-dimensional and beta-plane turbulence. *J. Fluid Mech.*, **228,** 321–342

Métais, O., Riley, J. J. and Lésieur, M. 1994 Numerical simulations of stably stratified rotating turbulence. Pp. 139–151 in *Stably-stratified flows—flow and dispersion over topography.* Eds. I.P. Castro and N. J. Rockiiff. Clarendon Press

Ogura, Y. and Phillips, N. A. 1962 A scale analysis of deep and shallow convection in the atmosphere. *J. Atmos. Sci.*, **19,** 173–179

Ooyama, K. 1971 A theory on parametrization of cumulus convection. *J. Meteorol. Soc. Jpn. (Special Issue)*, **49,** 744–756

Raymond, D. J. and Jiang, H. 1990 A theory for long-lived mesoscale convective systems. *J. Atmos. Sci.*, **47,** 3067–3077

Riley, J. J., Metcalfe, R. W. and Weissman, M. A. 1981 'Direct numerical simulations of homogeneous turbulence in density stratified fluids'. Pp. 79–112 in Proceedings of AIP conference on nonlinear properties of internal waves. Ed. B. J. West

Rotunno, R. Klemp, J. B. and Weisman, M. 1988 Structure and evolution of numerically simulated squall lines. *J. Atmos. Sci.*, **45,** 1990–2014.

Schubert, W. H., Hack, J. J., Silva-Dias, P. L. and Fulton, S. R. 1980 Geostrophic adjustment in an axisymmetric vortex. *J.Atmos. Sci.*, **37,** 1464–1484

Shutts G. J. and Gray, M. E. B. 1994 A numerical modelling study of the geostrophic adjustment process following deep convection. *Q. J. R. Meteorol. Soc.*, **120,** 1145–1178

Shutts G. J., Booth, M. and Norbury, J. 1988 A geometric model of balanced, axisymmetric flows with embedded penetrative convection. *J. Atmos. Sci.*, **45,** 2609–2621

Skamarock, W. C., Weisman M. L. and Klemp, J. B. 1994 Three-dimensional evolution of simulated, long-lived squall lines. *J. Atmos. Sci.*, **51,** 2563–2584

Vallis, G. K. 1985 Remarks on the predictability properties of two- and three-dimensional flow. *Q. J. R. Meteorol. Soc.*, **111,** 1039–1047

1996 Potential vorticity inversion and balanced equations of motion for rotating and stratified flows. *Q. J. R. Meteorol. Soc.*, **122,** 291–322

Van Zandt, T. E. 1982 A universal spectrum of buoyancy waves in the atmosphere. *Geophys. Res. Lett.*, **9,** 575–578

Yuan, L. and Hamilton, K. 1994 Equilibrium dynamics in a forced-dissipative f-plane shallow-water system. *J. Fluid Mech.*, **280,** 369–394